The AGNIFS survey: spatially resolved observations of hot molecular and ionized outflows in nearby active galaxies

Riffel, R.A.; Storchi-Bergmann, T.; Riffel, R.; Bianchin, M.; Zakamska, N.L.; Ruschel-Dutra, D.; ... ; Schönell, A.J.

Note: To cite this publication please use the final published version (if applicable).

The AGNIFS survey: spatially resolved observations of hot molecular and ionized outflows in nearby active galaxies

R. A. Riffel [1][*] T. Storchi-Bergmann,[2] R. Riffel [2] M. Bianchin [1] N. L. Zakamska [3,4]
D. Ruschel-Dutra [5] M. C. Bentz,[6] L. Burtscher,[7] D. M. Crenshaw,[6] L. G. Dahmer-Hahn,[8]
N. Z. Dametto,[9,10] R. I. Davies [11] M. R. Diniz [1] T. C. Fischer,[12] C. M. Harrison [13] V. Mainieri,[14]
M. Revalski,[15] A. Rodriguez-Ardila [16,17] D. J. Rosario [12] and A. J. Schönell[18]

[1]*Departamento de Física, Centro de Ciências Naturais e Exatas, Universidade Federal de Santa Maria, 97105-900, Santa Maria, RS, Brazil*
[2]*Instituto de Física, Universidade Federal do Rio Grande do Sul, Av. Bento Gonçalves 9500, 91501-970 Porto Alegre, RS, Brazil*
[3]*Department of Physics & Astronomy, Johns Hopkins University, Bloomberg Center, 3400 N. Charles St, Baltimore, MD 21218, USA*
[4]*Institute for Advanced Study, Einstein Dr, Princeton, NJ 08540, USA*
[5]*Departamento de Física, Universidade Federal de Santa Catarina, P.O. Box 476, 88040-900, Florianópolis, SC, Brazil*
[6]*Department of Physics and Astronomy, Georgia State University, 25 Park Place, Suite 605, Atlanta, GA 30303, USA*
[7]*Leiden Observatory, PO Box 9513, NL-2300 RA, Leiden, The Netherlands*
[8]*Shanghai Astronomical Observatory, Chinese Academy of Sciences, 80 Nandan Road, Shanghai 200030, China*
[9]*Instituto de Astrofísica de Canarias, E-38205 La Laguna, Tenerife, Spain*
[10]*Departamento de Astrofísica, Universidad de La Laguna, E-38206 La Laguna, Tenerife, Spain*
[11]*Max-Planck-Institut für Extraterrestrische Physik, Postfach 1312, D-85741, Garching, Germany*
[12]*AURA for ESA, Space Telescope Science Institute, 3700 San Martin Drive, Baltimore, MD 21218, USA*
[13]*School of Mathematics, Statistics and Physics, Newcastle University, NE1 7RU, UK*
[14]*European Southern Observatory, Karl-Schwarzschild-Strasse 2, Garching bei München, D-85748, Germany*
[15]*Space Telescope Science Institute, 3700 San Martin Drive, Baltimore, MD 21218, USA*
[16]*Laboratório Nacional de Astrofísica, Rua dos Estados Unidos, 154, 37504-364 Itajubá, MG, Brazil*
[17]*Instituto Nacional de Pesquisas Espaciais, Av. dos Astronautas, 1758 - Jardim da Granja São José dos Campos/SP - 12227-010, Brazil*
[18]*Instituto Federal de Educação, Ciência e Tecnologia Farroupilha, BR287, km 360, Estrada do Chapadão, 97760-000, Jaguari - RS, Brazil*

ABSTRACT

We present the hot molecular and warm ionized gas kinematics for 33 nearby ($0.001 \lesssim z \lesssim 0.056$) X-ray selected active galaxies using the H_2 2.1218 μm and Br γ emission lines observed in the K band with the Gemini near-infrared integral field spectrograph. The observations cover the inner 0.04–2 kpc of each active galactic nucleus at spatial resolutions of 4–250 pc with a velocity resolution of $\sigma_{inst} \approx 20$ km s^{-1}. We find that 31 objects (94 per cent) present a kinematically disturbed region (KDR) seen in ionized gas, while such regions are observed in hot molecular gas for 25 galaxies (76 per cent). We interpret the KDR as being due to outflows with masses of 10^2–10^7 and 10^0–10^4 M$_\odot$ for the ionized and hot molecular gas, respectively. The ranges of mass-outflow rates ($\dot{M}_{out}$) and kinetic power ($\dot{E}_K$) of the outflows are 10^{-3}–10^1 M$_\odot$ yr^{-1} and $\sim 10^{37}$–10^{43} erg s^{-1} for the ionized gas outflows, and 10^{-5}–10^{-2} M$_\odot$ yr^{-1} and 10^{35}–10^{39} erg s^{-1} for the hot molecular gas outflows. The median coupling efficiency in our sample is $\dot{E}_K/L_{bol} \approx 1.8 \times 10^{-3}$ and the estimated momentum fluxes of the outflows suggest they are produced by radiation-pressure in low-density environment, with possible contribution from shocks.

Key words: galaxies: active – galaxies: ISM – galaxies: Seyfert – techniques: imaging spectroscopy.

1. INTRODUCTION

The co-evolution of galaxies and their supermassive black holes (SMBHs) is supported by a large number of recent observational and theoretical studies (e.g. Magorrian et al. 1998; Ferrarese & Merritt 2000; Gebhardt et al. 2000; Di Matteo, Springel & Hernquist 2005; Murray, Quataert & Thompson 2005; Gültekin et al. 2009; Heckman & Kauffmann 2011; Kormendy & Ho 2013; Harrison 2017; Costa et al. 2018; Harrison et al. 2018; Storchi-Bergmann & Schnorr-Müller 2019; Caglar et al. 2020). This co-evolution is due to both feeding and feedback processes in active galactic nuclei (AGNs). The feedback processes comprise jets of relativistic particles emitted from the inner rim of the accretion disc, winds emanating from outer regions of the disc, and radiation emitted by the hot gas in the disc or by its corona (e.g. Elvis 2000; Frank, King & Raine 2002; Ciotti, Ostriker & Proga 2010), which is believed to play an important role in shaping galaxies in all mass ranges by quenching star formation in the hosts during cycles of nuclear activity (e.g. Di Matteo et al. 2005; Hopkins & Elvis 2010; Schaye et al. 2015; Silk 2017; Weinberger et al. 2017; Penny et al. 2018; Xu et al. 2022).

[*] E-mail: rogemar@ufsm.br

AGN feedback is strongly dependent on luminosity. For instance, quasars may inject enough energy into the galactic medium so that the wind can overcome the inertia of the gas in the galactic potential. In low-luminosity AGNs (LLAGNs), on the other hand, the outflows may not be powerful enough to affect the large-scale recent star formation in their hosts, in spite of some simulations predict that LLAGN can produce significantly feedback (Ward et al. 2022). In these LLAGNs, the connection seems to be rather related to the feeding process of the AGN—inflow of gas to the inner region—in the sense that recent studies have revealed an excess of intermediate-age stellar components, that can be interpreted as due to a delay between the onset of star formation and triggering of the AGN (e.g. Riffel et al. 2010, 2011; Storchi-Bergmann et al. 2012; Diniz et al. 2017; Mallmann et al. 2018; Burtscher et al. 2021; Riffel et al. 2022). Although AGN feedback may had a more profound impact on galaxy evolution at the cosmic noon ($z \approx 2$–3), AGN winds extending from hundreds of parsecs to a few kiloparsecs (e.g. Fischer et al. 2018; Förster Schreiber et al. 2019; Mingozzi et al. 2019; Kakkad et al. 2020; Santoro et al. 2020; Avery et al. 2021; Lamperti et al. 2021; Luo et al. 2021; Speranza et al. 2021; Vayner et al. 2021; Trindade Falcão et al. 2021; Deconto-Machado et al. 2022; Kakkad et al. 2022; Singha et al. 2022) are hardly spatially resolved at these distances. Thus, it is nearby galaxies that offer the only opportunity to test in detail the prescriptions used in models of galaxy and SMBH co-evolution.

Near-infrared (hereafter, near-IR) integral field spectroscopy (IFS) observations—and in particular with adaptive optics—provide resolutions of a few tens of parsecs in nearby AGN hosts, allowing to spatially resolve the gas emission structure and kinematics. Near-IR observations are less affected by dust extinction, probing more obscured regions than observations in optical bands. In addition, the near-IR spectra of AGN hosts typically present emission lines, both from hot molecular ($\sim$2000 K) and ionized gas (e.g. Rodríguez-Ardila et al. 2004; Riffel, Rodríguez-Ardila & Pastoriza 2006; Lamperti et al. 2017; Vivian et al. 2019; Riffel et al. 2021b; den Brok et al. 2022), allowing observations of multiphase AGN winds (e.g. Santoro et al. 2018; Ramos Almeida et al. 2019; Shimizu et al. 2019; Riffel 2021; Bianchin et al. 2022), fundamental to understand the role of AGN feedback in galaxy evolution.

The physical properties of outflows (e.g. mass-outflow rate and kinetic power) have been estimated using distinct methods and assumptions. These include using: (i) single-component fits of the line profiles and comparison with the rest-frame stellar velocity in single-aperture spectra (e.g. Kovačević-Dojčinović et al. 2022) and IFS (e.g. Ilha et al. 2019; Deconto-Machado et al. 2022); (ii) decomposition of the emission lines in multiple kinematic components using nuclear spectra (e.g. Perrotta et al. 2019) and *Hubble Space Telescope* (*HST*) long-slit data (e.g. Revalski et al. 2021), and IFS observations (e.g. Fischer et al. 2019; Bianchin et al. 2022; Kakkad et al. 2022, Speranza et al. 2022); and (iii) non-parametric measurements of the emission lines using both single aperture (e.g. Zakamska & Greene 2014) and IFS (e.g. Wylezalek et al. 2020; Ruschel-Dutra et al. 2021) data. A precise determination of outflow properties requires high-quality data to spatially and spectrally resolve the outflow component, as well as detailed photoionization models to calculate the gas masses and a correct determination of the gas density (e.g. Baron & Netzer 2019; Davies et al. 2020; Revalski et al. 2022). However, this procedure is time-demanding and hard to be applied for large samples. On the other hand, non-parametric measurements do not depend on details of the line-profile fitting procedure (e.g. choice of the number of components and their physical interpretations), can be applied to large samples and result in estimates of outflow properties consistent with those obtained with other methods (e.g. Ruschel-Dutra et al. 2021).

Here, we use non-parametric measurements to map the hot molecular and ionized gas kinematics in a sample of 33 X-ray selected AGN of the local Universe, observed with the Gemini near-infrared integral field spectrograph (NIFS). Our sample is drawn from Riffel et al. (2021b), who presented the NIFS data of 36 objects, 34 of them with extended emission observed in H_2 2.1218 μm and Br γ emission lines. In this previous work, we found that the H_2 emission is mainly due to thermal processes—X-ray heating and shocks—and its flux distribution is more extended than that of Br γ. In addition, regions of H_2 emission due to shocks are observed in about 40 per cent of the sample. The estimated masses of hot molecular and ionized gas in the inner 250-pc diameter are in the ranges 10^1–10^4 and 10^4–10^6 $M_\odot$, respectively. Finally, the only difference found between type 1 and type 2 AGN is that the nuclear emission-line equivalent widths of type 1 objects are smaller than in type 2, attributed to a larger contribution of hot dust emission to the galaxy continuum in the former. In this paper, we analyse the molecular and ionized gas kinematics using non-parametric measurements of the H_2 2.1218 μm and Br γ emission lines, define the kinematically disturbed region (hereafter KDR) as the region where the AGN significantly affects the gas kinematics (e.g. through AGN winds). The identification of KDRs allow to spot locations where the gas is strongly impacted by outflows, and estimate the outflow properties for both gas phases.

This work is organized as follows: Section 2 summarizes the sample properties, observations, and measurement procedures. Section 3 presents the selection criteria to identify KDRs and regions where the gas motions are dominated by the gravitational potential of the galaxies. In Section 4, we estimate the outflow properties, which are discussed in Section 5. Our conclusions are listed in Section 6. Additional maps of the gas kinematics for individual objects are included as Supplementary Materials.

2. DATA AND MEASUREMENTS

2.1 The sample and data

The sample used in this work is the same from Riffel et al. (2021b), which is composed of 36 AGNs observed with Gemini NIFS in the *K* band. In short, the sample was defined by cross-correlating the list of objects included in the 105-month catalogue of the *Swift Burst Alert Telescope* (*BAT*) survey (Oh et al. 2018) at redshifts $z < 0.12$, with the objects from the Gemini Science Archive with *K*-band NIFS data available. As the main aim of this paper is to identify KDRs by the AGN, we have excluded the advanced stage merger NGC 6240 from the analysis performed in this study, as the disturbed gas may be mainly due to shocks from the interaction process. This object has been extensively studied, including by near-IR IFS (Ilha, Bianchin & Riffel 2016; Müller-Sánchez et al. 2018). In addition, no extended H_2 or Br γ emission is detected with the NIFS data for two galaxies in the sample of Riffel et al. (2021b)—NGC 3393 and Mrk 352. Thus, in this paper, we present the molecular and ionized gas kinematics for 33 AGN hosts, 16 classified as type 2 AGN and 17 as type 1 (Oh et al. 2018).

In Fig. 1, we present the AGN bolometric luminosity (top panel) and redshift (bottom panel) distributions of our sample. The AGN bolometric luminosities are obtained from the hard X-ray (14–195 keV) intrinsic luminosities presented in Ricci et al. (2017) using the relation $\log L_{\rm bol} = 0.0378(\log L_{\rm X})^2 - 2.03\log L_{\rm X} + 61.6$ from (Ichikawa et al. 2017). For Mrk607 and Mrk1066, which are not in the sample of Ricci et al. (2017), we use the observed X-ray
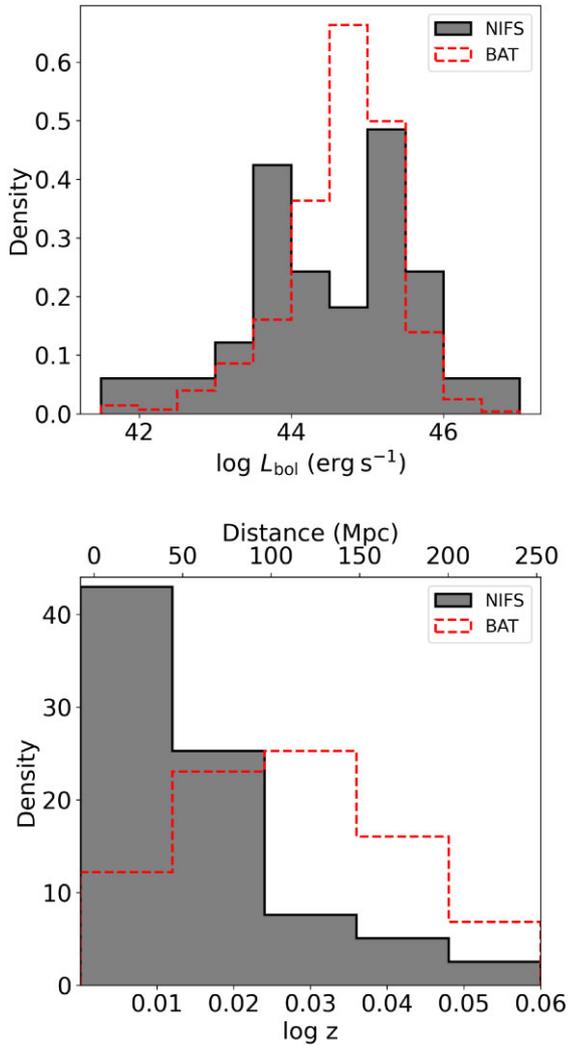
Figure 1. AGN bolometric (top panel) and redshift (bottom panel) distribution of our sample (grey) and *BAT* survey (red; Oh et al. 2018) for the same redshift range.

luminosities from Oh et al. (2018). For most galaxies we adopt distances based on their redshifts, except for those with accurate distance determinations: NGC 3227 (20.5 Mpc; Tonry et al. 2001), NGC 4051 (16.6 Mpc; Yuan et al. 2021), NGC 4151 (15.8 Mpc; Yuan et al. 2020), NGC 4258 (7.6 Mpc; Reid, Pesce & Riess 2019), NGC 4395 (4.0 Mpc; Thim et al. 2004), and NGC 6814 (21.65 Mpc; Bentz et al. 2019).

The comparison of the luminosity and redshift distributions of our sample with those from the whole 105-month *BAT* catalogue (Oh et al. 2018) for the same redshift range (Fig. 1) shows that these distributions are distinct. In comparison to the *BAT* catalogue, our sample is biased to lower redshifts and distinct luminosity distribution. The results presented in this paper should not be considered as statistically significant for a complete, volume-limited sample of nearby AGN. The different luminosity and redshift distributions between the BAT catalogue and our sample are due to the fact that we have used archival data with observations obtained to address distinct scientific goals. However, it should be mentioned that the sample used in this work provides one of the largest comparisons of hot molecular and ionized gas kinematics available in the literature, which can provide important information about the

emission structure and gas dynamics in these phases in the central region of AGN hosts.

The data were obtained with the Gemini NIFS (McGregor et al. 2003), which has a square field of view of 3×3 arcsec^2. The angular resolution of the observations is in the range $0\overset{''}{.}11$–$0\overset{''}{.}44$ and velocity resolution of $\sigma_{\mathrm{inst}} \sim 20$ km s^{-1} (see Riffel et al. 2018b, 2021b). The data reduction followed the standard procedures, as described in Riffel et al. (2017), resulting in a single data cube for each galaxy at angular sampling of $0\overset{''}{.}05 \times 0\overset{''}{.}05$. More details about the sample, observational strategy, and data reduction can be found in Riffel et al. (2017, 2018b, 2021b).

2.2 Measurements

We characterize the hot molecular and ionized gas kinematics by measuring the W_{80}, V_{peak}, and V_{cen} parameters for the H$_2$ 2.1218 µm and Br γ emission lines, respectively. The W_{80} is defined as the smallest width of the line that contains 80 per cent of its total flux and has been used to look for signatures of ionized gas outflows in AGN hosts (Zakamska & Greene 2014; McElroy et al. 2015; Wylezalek et al. 2017, 2020; Kakkad et al. 2020; Riffel et al. 2020). V_{peak} is the velocity corresponding to the peak of the emission line, which is expected to trace emission from gas in the galaxy disc, while V_{cen} is the centroid velocity, which is expected to be different from V_{peak} for asymmetric profiles. These properties are computed by using the fits of the spectra performed by Riffel et al. (2021b) using the IFSCUBE code (Ruschel-Dutra 2020; Ruschel-Dutra et al. 2021), where the H$_2$ 2.1218 µm and Br γ emission lines are represented by up to three Gaussian components and the underlying continuum is reproduced by a first-order polynomial function. The measurements of W_{80} and V_{cen} are also obtained with the IFSCUBE code, while V_{peak} is obtained directly from the modelled spectra by computing the velocity corresponding to the maximum flux value within a spectral window of 1500 km s^{-1} centred at the peak of each emission line.

In Fig. 2, we present examples of the resulting line flux and kinematic maps. Besides the maps for W_{80}, V_{peak}, and V_{cen} for H$_2$ 2.1218 µm and Br γ, we also present the flux maps for these emission lines, obtained by integrating the line profiles within a spectral window of 1500 km s^{-1} centred at each emission line and a continuum image in the K band—already presented in Riffel et al. (2021b), as well as maps identifying the KDRs and virially dominated region (VDRs; see Section 3). In the bottom row of Fig. 2 we also present histograms for the distributions of W_{80} values and residual velocities, V_{res}, defined as $V_{\mathrm{res}} = V_{\mathrm{cen}} - V_{\mathrm{peak}}$ for both emission lines, as well as representative line profiles that will be discussed in the forthcoming sections. In all maps, we masked out regions where the peak of the line profile is not above three times the noise in the neighbouring continuum. These regions are shown as grey areas in the maps.

3. THE KDR

Ionized outflows have been extensively studied in AGN hosts, mostly by using the [O III]λ5007 emission line as its tracer (e.g. Zakamska & Greene 2014; Wylezalek et al. 2017, 2020; Kakkad et al. 2020; Riffel et al. 2020; Ruschel-Dutra et al. 2021). The W_{80} parameter can be used to identify the KDR, defined as the region where the AGN significantly affects the gas kinematics (e.g. through AGN winds or *in situ* acceleration of the clouds via radiation pressure). Usually $W_{80} > 600$ km s^{-1}, observed in the [O III]λ5007 line is associated with ionized outflows in quasars (e.g. Kakkad et al. 2020), while in LLAGN hosts $W_{80} > 500$ km s^{-1} may already be tracing the KDR
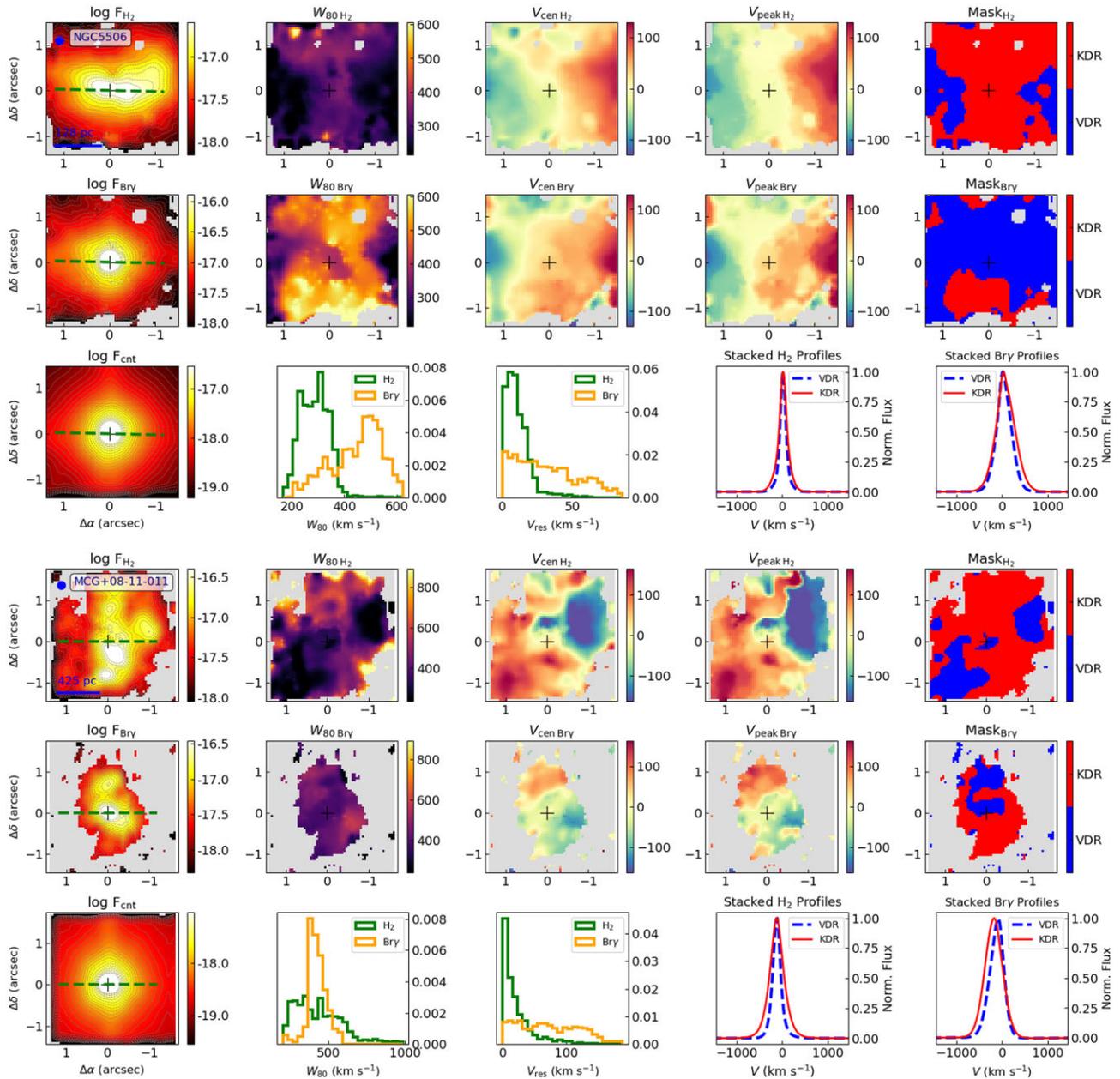
Figure 2. Examples of maps for NGC 5506 (top panels) and MCG + 08-11-011 (bottom panels). For each galaxy, the first row shows the results for the H_2 2.1218 μm and second row show results for the Br γ emission line. From left to right: Emission-line flux distribution, W_{80}, V_{cen}, V_{peak}, and a 'kinematic map' identifying the KDR in red and the VDR in blue. The colour bars show fluxes in $erg\,s^{-1}\,cm^{-2}\,spaxel^{-1}$ and velocities in $km\,s^{-1}$. The grey areas identify locations where the emission-line amplitude is below three times the continuum noise amplitude (3σ). The bottom rows show a K-band continuum image in $erg\,s^{-1}\,cm^{-2}\,\text{Å}^{-1}\,spaxel^{-1}$, the density distributions of W_{80} and $V_{res} = |V_{cen} - V_{peak}|$ and stacked profiles of the H_2 and Br γ emission lines from the VDR and KDR. Stacked profiles for the KDR are presented only if it corresponds to at least 10 per cent of the spaxels with detected emission. The green dashed lines in the leftmost panels show the orientation of the major axis of the large-scale disc, as presented in Riffel et al. (2021b). In all maps, north is up and east is to the left.

emission and consistent with radiatively or mechanically driven AGN outflows (e.g. Wylezalek et al. 2020). The justification for the choice of this threshold is that even for the deepest galaxy gravitational potential of the most massive galaxies, normal orbital velocities and velocity dispersions correspond to lower W_{80} values.

The W_{80} cuts mentioned above are determined using the [O III]λ5007 emission as a tracer of the KDR, and different cuts may be used for distinct tracers, considering the multiple gas phases in the

KDR. The Br γ emission line is more sensitive to star formation for which narrower profiles are usually observed, compared to [O III] which is a better tracer of the highest ionization gas. Thus, if an outflow component is superimposed to a disc component, the W_{80} cutoff value for Br γ is expected to be smaller than that for [O III]. Similarly, the H_2 near-IR emission from the inner region of nearby Seyfert galaxies originates mostly from gas rotating in the disc, also resulting in narrower line profiles compared to those
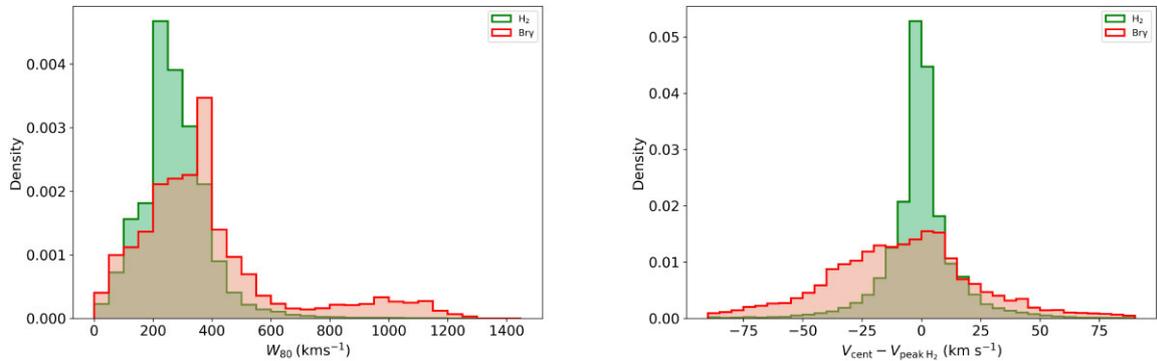
Figure 3. Left-hand panel: Br γ (in red) and H$_2$ 2.1218 µm (in green) W_{80} distributions for our sample in bins of 50 km s^{-1} using measurements in all spaxels. Right-hand panel: Br γ (in red) and H$_2$ 2.1218 µm (in green) residual centroid velocity distributions for our sample in bins of 5 km s^{-1}.

from ionized gas emission lines (e.g. Riffel et al. 2018b). Fig. 3 presents the W_{80} distributions of the H$_2$ 2.1218 µm (in green) and Br γ (in red) emission lines for our sample. Overall, higher W_{80} values are observed for Br γ than for H$_2$ 2.1218 µm, confirming previous results. In addition, the Br γ W_{80} distribution clearly presents a tail of high values. A less-prominent tail is also observed in the H$_2$ distribution, but with smaller values. Furthermore, a more accurate way of identifying the KDR requires defining different W_{80} thresholds not only for each line but also for each object.

For the definition of the KDR we also use the galaxies nuclear spectra to measure the emission-line and stellar kinematics. We extract a spectrum within a circular aperture of 0.''25 radius centred at the peak of the continuum emission. The size of the aperture is comparable to the angular resolution of the data (Riffel et al. 2021b) and so, the measured kinematics is representative of the nucleus of each galaxy. We measure the stellar line-of-sight velocity distribution of each galaxy by fitting the CO absorption band-heads ($\sim$2.29–2.40 µm—rest wavelengths) with the penalized pixel-fitting PPXF method (Cappellari & Emsellem 2004; Cappellari 2017) using the Gemini library of late-spectral-type stars observed with the Gemini near-infrared spectrograph (GNIRS) Integral Field Unit (IFU) and NIFS (Winge, Riffel & Storchi-Bergmann 2009). We were able to obtain measurements of the stellar kinematics for 14 objects (Mrks 1066, 348, and 607 and NGCs 1052, 1125, 1241, 2110, 3227, 3516, 4051, 4258, 4388, 5899, and 788) in our sample. For the other objects the CO absorption bands are not detected (or are too weak), mainly due to the dilution of the bands by dust emission (Burtscher et al. 2015; Riffel et al. 2017). We measure the emission-line properties using the same procedure described in the previous section, using the IFSCUBE code.

The near-IR H$_2$ emission in nearby AGN hosts is usually dominated by emission of gas in rotation in the plane of the galaxy (e.g. Hicks et al. 2013; Mazzalay et al. 2014; Riffel et al. 2018b); thus, the peak velocity measured from the H$_2$ 2.1218 µm is expected to be similar to that of the stars. Indeed, the comparison between the nuclear H$_2$ peak velocities and the stellar velocities show that they are consistent with an average difference of $\langle V_{\text{peak H}_2} - V_{\text{stars}} \rangle = -6$ km s^{-1}, which is within NIFS velocity resolution of $\sim$50 km s^{-1}, and a standard deviation of 34 km s^{-1}. The velocity differences are in the range from -45 ± 13 km s^{-1} (for NGC 1241) and 70 ± 9 km s^{-1} (for NGC 1052). This indicates that both the peak H$_2$ 2.1218 µm velocity and stellar velocity trace the systemic velocities of the galaxies and that $V_{\text{peak H}_2}$ can be used as a proxy of the bulk velocity of the VDR.

If the gas motions are dominated by the gravitational potential, it is expected that the velocity dispersion (measured here by the W_{80} parameter) decreases with the distance to the nucleus, so that the nuclear value can be used as the maximum velocity dispersion that can be attributed to the gravitational potential. We fit the emission-line profiles in the nuclear spectra by a single Gaussian curve. In order to minimize the inclusion of outflows in this nuclear spectrum, we restrict the centroid velocity of the Gaussian to differ by at most 50 km s^{-1} from the stellar velocity (50 km s^{-1} is roughly the NIFS velocity resolution—full width at half-maximum). If this condition does not apply, we include another Gaussian component in the fit and adopt as representative of the orbital motion the one with centroid velocity closer to the stellar one. For galaxies with no stellar kinematics measurements, we use the peak H$_2$ 2.1218 µm velocity as reference. If the line profile is well reproduced by a single Gaussian function, we use its W_{80} plus the corresponding uncertainty as a threshold to define the KDR. Spaxels with W_{80} values larger than this threshold are associated to the KDR, while spaxels with smaller values are attributed to virialized gas motions, corresponding to the VDR. In Fig. 4, we present examples of the line-profile fits and in Table 1 we show the maximum W_{80} values attributed to motions under the gravitational potentials for each galaxy.

In some cases, instead of a significant enhancement of the gas velocity dispersion, an outflow produces only a deviation of the centroid velocity of the gas with respect to that corresponding to the galaxy rest frame. This may occur, for instance, in a bipolar outflow launched from the galaxy nucleus at an angle almost perpendicular to the galaxy disc, so that the outflow just weakly interacts with the gas in the disc (e.g. Riffel, Storchi-Bergmann & Winge 2013; Bianchin et al. 2022). In order to account for this possibility, we consider that the V_{peak} parameter traces virially dominated motion and compute the residual velocity $V_{\text{res}} = |V_{\text{cen}} - V_{\text{peak}}|$. As the H$_2$ is a better tracer of the emission of the disc, we use the V_{peak} measured for the H$_2$ 2.1218 µm to compute the V_{res} for both lines. If $V_{\text{res}} > 50$ km s^{-1}, we assume that the gas motions are not dominated by the gravitational potential. We point out that only a few spaxels are selected using this criteria. The fraction of spaxels with $V_{\text{res}} > 50$ km s^{-1} correspond to only 1 per cent of the total number of spaxels for the H$_2$ and about 4 per cent for the Br γ.

In summary, throughout this paper, locations where W_{80} are larger than the values listed in Table 1 plus their uncertainties or $V_{\text{res}} > 50$ km s^{-1} are identified as the gas KDR. The KDR is assumed to be produced by outflows. Other regions are identified as the VDRs. In
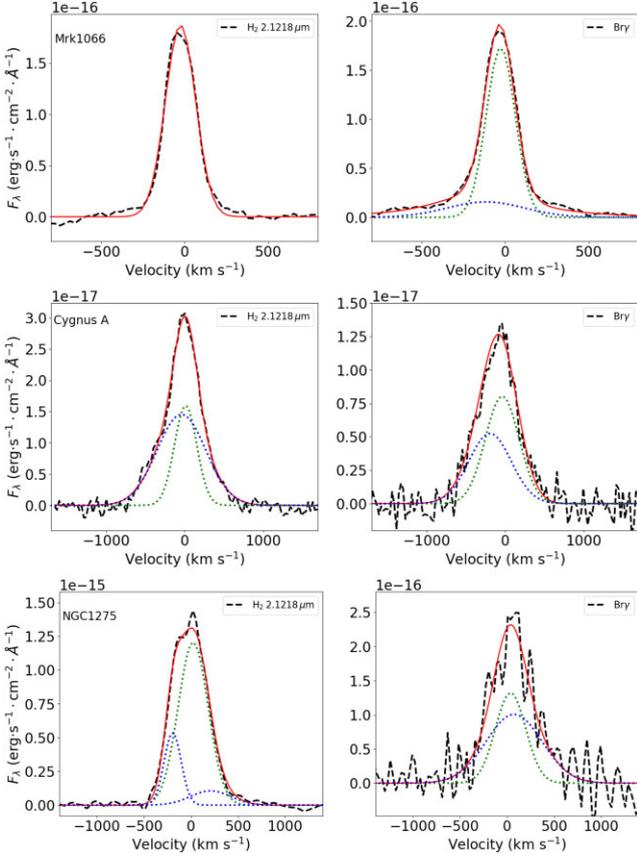
Figure 4. Examples of fits of the nuclear emission-line profiles, within an aperture of $0.''25$ radius. Left-hand panels show the fits of the H_2 2.1218 µm and right-hand panels show results for the Br γ for Mrk 1066 (top panel), Cygnus A (middle panel), and NGC 1275 (bottom panel). The observed profiles are shown in black and the best-fitting model in red. If more than one Gaussian function is used to represent the line profile, the dotted green line shows the component attributed to VDR, while the blue dotted lines represents the KDR emission.

the next section, we derive the outflow properties and discuss their uncertainties.

4. PROPERTIES OF THE OUTFLOWS

The origin of the KDR in central region of AGN hosts may be due to gas outflows (e.g. Wylezalek et al. 2020; Ruschel-Dutra et al. 2021; Deconto-Machado et al. 2022) and thus, we can use the flux and kinematic measurements to determine the properties of the hot molecular and ionized gas outflows, traced by the H_2 and Br γ emission lines, respectively. In the two bottom-right panels for each galaxy in Fig. 2, we present stacked emission-line profiles for the KDR (in red) and VDR (blue). These profiles were constructed by summing up all spaxels of each region using the peak velocity of the line as reference. Such profiles are shown for all objects in the Supplementary Material. In order to avoid possible spurious measurements, we only plot the stacked profile for the KDR if this region corresponds to at least 10 per cent of the spaxels with detection of the corresponding emission line. As expected (by definition) the profiles from the KDR are broader and in several cases present distinctly different peak velocities than those from the VDR.

We find that 31 galaxies (94 per cent) present at least 10 per cent of the spaxels in the KDR considering only spaxels with detected

Table 1. W_{80} values for the disc component in our sample (see text) for an aperture of $0.''25$ radius centred at the peak of the continuum emission. (1) Object, (2) Number of Gaussian functions used to represent the H_2 2.1218 µm emission line, (3) W_{80} measured for the H_2 from the Gaussian component that represents the disc, and (4) its uncertainty. (5)–(7) Same as (2)–(4), but for the Br γ emission line. We consider spaxels with W_{80} values larger than the nuclear values plus their uncertainties as a signature of kinematically disturbed gas. For objects with no nuclear emission, we adopt a W_{80} threshold of 500 km s^{-1} as a lower limit to identify the KDR, following Wylezalek et al. (2020). We identify these objects with the superscript *.

(1)	(2)	(3)	(4)	(5)	(6)	(7)
		H_2 2.1218 µm			Br γ	
		Type 2				
NGC788	1	197	30	2	227	29
NGC1052	1	345	36	1	329	65
NGC1068	1	200	50	1	444	68
NGC1125	2	212	37	2	228	30
NGC1241	1	262	29	1	305	41
NGC2110	2	347	47	2	230	61
NGC4258	1	294	47	1	521	52
NGC4388	1	226	28	1	220	29
NGC5506	1	197	42	2	580	33
NGC5899	1	239	26	2	366	43
Mrk3	2	275	55	2	330	47
Mrk348	2	156	54	2	167	69
Mrk607	3	237	43	3	350	43
Mrk1066	1	232	26	2	222	27
ESO578−G009	–	500*	–	–	500*	–
Cygnus A	2	365	35	2	551	42
		Type 1				
NGC1275	3	408	26	2	412	45
NGC3227	2	224	34	2	356	42
NGC3516	2	193	54	1	220	53
NGC4051	1	158	32	2	211	38
NGC4151	1	355	91	1	393	41
NGC4235	1	371	52	–	500*	–
NGC4395	1	84	24	1	101	25
NGC5548	1	311	46	2	384	64
NGC6814	1	161	30	2	291	43
Mrk79	1	315	48	1	250	53
Mrk509	–	500*	–	–	500*	–
Mrk618	1	199	46	1	360	43
Mrk766	1	155	38	2	169	32
Mrk926	2	201	52	2	382	52
Mrk1044	–	500*	–	–	500*	–
Mrk1048	2	191	44	1	148	47
MCG + 08-11-011	1	279	43	1	445	43

Br γ emission. For the H_2, the number of objects with more than 10 per cent of the spaxels in the KDR is 25 (76 per cent). We estimate the outflow properties only for these objects, in each gas phase.

4.1 Estimates of the outflows properties

We estimated the mass of hot H_2 and H II using the fluxes of the H_2 2.1218 µm and Br γ emission lines, respectively. The mass of hot molecular gas can be derived by

$$\left(\frac{M_{H_2}}{M_{\odot}}\right) = 5.0776 \times 10^{13} \left(\frac{F_{H_2\,2.1218}}{\mathrm{erg\,s^{-1}\,cm^{-2}}}\right)\left(\frac{D}{\mathrm{Mpc}}\right)^2, \quad (1)$$

where $F_{H_2\,2.1218}$ is the H_2 2.1218 µm emission-line flux and D is the distance to the galaxy. Local thermal equilibrium is assumed with

an excitation temperature of 2000 K (e.g. Scoville et al. 1982; Riffel et al. 2014).

The mass of ionized gas is obtained by

$$\left(\frac{M_{\mathrm{HII}}}{\mathrm{M_\odot}}\right) = 3 \times 10^{19} \left(\frac{F_{\mathrm{Br}\gamma}}{\mathrm{erg\,cm^{-2}\,s^{-1}}}\right)\left(\frac{D}{\mathrm{Mpc}}\right)^2 \left(\frac{N_e}{\mathrm{cm^{-3}}}\right)^{-1}, \quad (2)$$

where $F_{\mathrm{Br}\gamma}$ is the Br γ flux and N_e is the electron density (Osterbrock & Ferland 2006; Storchi-Bergmann et al. 2009). We adopt an electron density of $N_e = 1000\,\mathrm{cm^{-3}}$, which is a typical value measured in AGN hosts from the [S II]$\lambda\lambda$6717,6730 lines (e.g. Dors et al. 2014, 2020; Brum et al. 2017; Freitas et al. 2018; Kakkad et al. 2018).

Many assumptions are needed to estimate the properties of outflows, which can lead to different results. These properties are affected mainly by the choice of geometries and densities (e.g. Harrison et al. 2018; Baron & Netzer 2019; Davies et al. 2020; Kakkad et al. 2020, 2022; Lutz et al. 2020; Revalski et al. 2021, 2022; Ruschel-Dutra et al. 2021). Here, we estimate the mass of the gas in the outflow (M_{out}) by

$$M_{\mathrm{out}} = \sum_i M_{\mathrm{out}}^i, \quad (3)$$

where the sum is done over all spaxels whose emission is dominated by the outflow as defined above and M_{out}^i is the mass of the outflow calculated for each spaxel i, using equations (1) and (2) for the molecular and ionized gas, respectively. Following Ruschel-Dutra et al. (2021), to compute the masses of the gas in the outflow, instead of using the total flux of the emission lines from the spaxels in the KDR (F_{KDR}), we use only the fraction of the flux corresponding to absolute velocities larger than $W_{80}/2$ from the peak velocity. Then, we characterize the outflows in two different ways: (i) adopting a spherical shell geometry and (ii) obtaining radial profiles of the properties and then using them to estimate their peak values. These outflow properties are calculated as follows:

(i) Spherical geometry: global outflow properties
(ii) Radial profiles: peak outflow properties

4.1.1 *Spherical geometry: global outflow properties*

In this method, we estimate the global or integrated outflow properties.

(i) Velocity of the bulk of the outflow (V_{out}), defined as

$$V_{\mathrm{out}} = \frac{\langle W_{80\,\mathrm{KDR}} F_{\mathrm{KDR}}\rangle}{\langle F_{\mathrm{KDR}}\rangle}, \quad (4)$$

which is an average velocity over the region dominated by outflows where $W_{80\,\mathrm{KDR}}$ and F_{KDR} are the W_{80} values and fraction of the flux corresponding to absolute velocities larger than $W_{80}/2$ from the peak velocity of the corresponding emission lines for spaxels in the KDR.

(ii) Radius of the bulk of the outflow (R_{out}), defined as

$$R_{\mathrm{out}} = \frac{\langle R_{\mathrm{KDR}} F_{\mathrm{KDR}}\rangle}{\langle F_{\mathrm{KDR}}\rangle}, \quad (5)$$

where R_{KDR} are the distances of outflow-dominated spaxels from the galaxy's nucleus.

(iii) Mass-outflow rate computed by assuming a spherical geometry ($\dot{M}_{\mathrm{out}}^{\mathrm{b}}$), given by

$$\dot{M}_{\mathrm{out}}^{\mathrm{b}} = \frac{M_{\mathrm{out}} V_{\mathrm{out}}}{R_{\mathrm{out}}}. \quad (6)$$

(iv) Kinetic power of the outflow for a spherical geometry ($\dot{E}_{\mathrm{out}}^{\mathrm{b}}$), given by

$$\dot{E}_{\mathrm{out}}^{\mathrm{b}} = \frac{1}{2}\dot{M}_{\mathrm{out}}^{\mathrm{b}} V_{\mathrm{out}}^2. \quad (7)$$

4.1.2 *Radial profiles: peak outflow properties*

In this method, we calculate the properties as a function of distance from the nucleus and adopt as mass-outflow rate and power their peak values. We compute the mass-outflow rates within circular apertures of $0\farcs25$ width centred at the nucleus considering only spaxels whose line emission are dominated by the outflow component. For each shell, the mass rate [$\dot{M}_{\mathrm{out}}^{\mathrm{sh}}(r)$] and kinetic power [$\dot{E}_{\mathrm{out}}^{\mathrm{sh}}(r)$] of the outflow are computed by

$$\dot{M}_{\mathrm{out}}^{\mathrm{sh}}(r) = \frac{M_{\mathrm{out}}^{\mathrm{sh}} V_{\mathrm{out}}^{\mathrm{sh}}}{\Delta R}, \quad (8)$$

and

$$\dot{E}_{\mathrm{out}}^{\mathrm{sh}}(r) = \frac{1}{2}\dot{M}_{\mathrm{out}}^{\mathrm{sh}}(r)\left(V_{\mathrm{out}}^{\mathrm{sh}}\right)^2, \quad (9)$$

respectively. In these equations, r corresponds to the distance of the centre of the shell from the nucleus, $M_{\mathrm{out}}^{\mathrm{sh}}$ is the mass of the gas in the outflow in the shell obtained using equations (1) and (2), $V_{\mathrm{out}}^{\mathrm{sh}}$ is the outflow velocity defined as the median of the W_{80} values within the shell, and ΔR is the width of the shell ($0\farcs25$). Then, we define the outflow properties using the parameters below.

(i) Radius corresponding to the peak of the outflow (R_{peak}): The R_{peak} is defined as the radius where the mass-outflow rate radial profile reaches its maximum value. In Fig. 5, we present the resulting radial profiles for the ionized and molecular gas mass-outflow rate.

(ii) Maximum value of the mass-outflow rate ($\dot{M}_{\mathrm{peak}}$): It is defined as the peak of the values computed within circular apertures of $0\farcs25$ width (i.e. the maximum value of $\dot{M}_{\mathrm{out}}^{\mathrm{sh}}$).

(iii) Maximum value of the kinetic power of the outflow ($\dot{E}_{\mathrm{peak}}$): It is defined as the peak of the values computed circular apertures of $0\farcs25$ width (i.e. the maximum value of $\dot{E}_{\mathrm{out}}^{\mathrm{sh}}$).

In Fig. 5, we present the radial profiles of the mass-outflow rates in ionized (top panel) and hot molecular (bottom panel) gas. For most galaxies, the radial distribution of the mass-outflow rates in both molecular and ionized gas shows an increase with radius from the nucleus until reaching a maximum value at R_{peak}, then decreasing with radius. A similar behaviour was obtained by Revalski et al. (2021) for six luminous Seyfert galaxies (including NGC 1068, NGC 4151, and Mrk 3) based on observations of the [O III] emission line using long-slit spectra obtained with the space telescope imaging spectrograph (STIS) and accurate determinations of radial density profiles.

4.2 Uncertainties

The uncertainties in the properties of AGN outflows are usually high because of the number of assumptions that have to be made to estimate them, such as the geometry, the electron density, and velocity of the outflow. The electron density represents one of the major source of uncertainties in computing the mass-outflow rates in ionized gas due to different assumptions or tracers used to measure it. Depending on tracer of the electron density used, uncertainties of approximately one order of magnitude are expected for the derived mass-outflow rates, as extensively discussed in recent works (e.g. Baron & Netzer 2019; Davies et al. 2020; Revalski et al. 2022).

The electron density in the AGN narrow-line region is a strong function of the distance to the nucleus and calculating the masses of ionized gas require multicomponent photoionization models to reproduce the observed emission-line intensities, as done by Revalski et al. (2022) for a sample of nearby Seyfert galaxies using *HST* STIS spectra. These authors found that using a constant density value of 10^2 cm^{-3} overestimates the mass of ionized gas, while adopting a value of 10^3 cm^{-3} results in an agreement within ±1 dex between the masses estimated from H recombination lines and those obtained from photoionization models. As aforementioned, in this work, we adopt $N_e = 1000$ cm^{-3}, which is a typical value for AGN hosts using the [S II] doublet (e.g. Dors et al. 2014, 2020; Perna et al. 2017; Freitas et al. 2018; Kakkad et al. 2018), and thus the expected uncertainty regarding the density choice is ∼1 dex in the outflow properties.

The uncertainty associated to the geometry of the outflow is smaller, with distinct geometries (e.g. conical and shells) resulting in overall similar values of the mass-outflow rates, and with typical standard deviations of the differences of <0.5 dex between the estimates using distinct geometries (e.g. Kakkad et al. 2022).

Another source of uncertainty in the estimate of outflow properties using spatially resolved observations is associated to the selection criteria of the outflow dominated spaxels and the emission-line fluxes used to compute the mass of gas in the outflow. In order to estimate the effect of different assumptions, we estimate the global mass-outflow rates using three sets of assumptions. The assumptions are the following: *Method 1*—we assume that spaxels with W_{80} larger than the values presented in Table 1 are associated to outflows as in the calculation described in Section 4 (which we will refer to as the *adopted method* for comparison purposes), but we use the total line flux of the spaxel instead of only the fluxes of its wings as done in Section 4. A fraction of the emission-line flux may be due to the emission of the gas in the disc (at lower velocities), resulting in an overestimation of the gas mass in the outflow. Thus, *method 1* likely results in upper limits for the outflow properties. *Method 2*—the spaxels corresponding to outflows are selected using a single W_{80} threshold of 500 km s^{-1} as defined by Wylezalek et al. (2020), and the total flux of the line in each spaxel is used to compute the mass of gas. *Method 3*—the same W_{80} threshold of *method 2* is used, and the mass of ionized gas is calculated using the flux corresponding to absolute velocities larger than $W_{80}/2$ from the peak velocity of the corresponding emission line. These assumptions will likely result in a lower limit of the mass-outflow rate, as it does not include lower velocity outflows.

In Fig. 6, we present the comparison among the mass-outflow rates in ionized (left-hand panel) and hot molecular (right-hand panel) gas derived using the different set of assumptions, for each object. The mean differences between the maximum and minimum values are 1.0 ± 0.5 dex for the ionized gas and 0.7 ± 0.4 dex for the hot molecular gas. The highest discrepancies are of about two orders of magnitude for the ionized gas and one order of magnitude for the molecular gas, with the *adopted method* resulting in values between the maximum and minimum estimates for most objects.

With these caveats in mind, we summarize the outflow properties and compare with values available in the literature, most of which share the same sources of uncertainty in measurements as ours.

4.3 Summary of derived outflow properties and comparison with the literature

In Tables 2 and 3, we present the derived properties of the ionized and molecular outflows, respectively. The uncertainties in the outflow parameters quoted in the table are estimated by propagating the

uncertainties in the fluxes of the H$_2$ 2.1218 μm and Br γ emission lines, the uncertainties in the radius (estimated as the standard error of the radii of individual spaxels in the KDR) and velocity of the outflow (estimated as the standard error of W_{80} values in the KDR). This uncertainties can be considered as lower limits, as systematic errors regarding the assumptions (e.g. densities and geometry) used to calculate the outflow properties may be the dominant source of uncertainties in deriving outflow properties, as discussed in Section 5. The masses of ionized gas in the outflow are in the range of 10^3–10^7 M$_\odot$, while the molecular outflows show masses in the range of 10^1–10^4 M$_\odot$. Fig. 7 shows the distributions of the mass fraction of the gas in the outflow relative to the total mass of molecular and ionized gas ($f_{out} = M_{out}/M_{gas}$), obtained using equation (1) and (2). The mass of the gas in the outflow is estimated by considering only spaxels from the KDR, while the total gas masses are obtained by summing the contributions of all spaxels within the observed field of view with detected emission. For galaxies with no detected outflows, we assume $f_{out} = 0$. The f_{out} in ionized and molecular gas are listed in Tables 2 and 3, respectively. For most galaxies, the amount of outflowing gas corresponds to <30 per cent of the total gas reservoir in the central region of the galaxies, both in ionized and molecular gas.

In the top panels of Fig. 8, we show the plots of the mass-outflow rates obtained for the ionized (left-hand panel) and molecular gas against the AGN bolometric luminosity. For each object, we present estimates using the two approaches described above, for the global properties of the outflow (red circles) and peak value of the radial profile (blue diamond). The black points represent a compilation of measurements available in the literature for ionized outflows for nearby AGN, adopting various values of electron density for the outflow. These points include estimates for LLAGN based on SDSS-III spectra using densities based on the ionization parameter (Baron & Netzer 2019), luminous Seyferts based on nuclear spectra using densities measurements from auroral and transauroral lines (Davies et al. 2020) and on long-slit *HST* spectra and photoionization models (Revalski et al. 2021), and nearby Quasi-Stellar Objects (QSOs) based on *HST* spectra and photoionization models (Trindade Falcão et al. 2021).

As discussed in recent works, the choice of the method used to estimate the density of ionized outflows is one of the main sources of uncertainty to estimate their mass-outflow rates (Baron & Netzer 2019; Davies et al. 2020; Revalski et al. 2022), resulting in values that can differ by approximately one order of magnitude. For example, the most common method used in the optical to estimate the electron density, based on the [S II]$\lambda\lambda$6717,6731 doublet, provides values significantly lower than the real densities of ionized outflows (Davies et al. 2020). In Fig. 8, we include mass-outflow rates from Ruschel-Dutra et al. (2021), Deconto-Machado et al. (2022), and Kakkad et al. (2022, for their estimates using a circular 3-arcsec diameter aperture), estimated using densities based on the [S II] lines, measured from spatially resolved spectra. These estimates are shown as grey triangles.

In addition, a wide range of densities—mostly in the range of 10^2–10^4 cm^{-3} (e.g. Liu et al. 2013; Diniz et al. 2019; Kakkad et al. 2020)—have been adopted to determine the properties of outflows over the last decade, in case it cannot be directly estimated from the data used. As can be seen in equation (2), the mass of ionized gas is inversely proportional to the electron density and thus, we scale the mass outflow-rates from the literature to the adopted density in this work ($N_e = 1000$ cm^{-3}) and show them as grey crosses in Fig. 8. This compilation is available as Supplementary Material and includes the estimates presented in Fiore et al. (2017), and based on
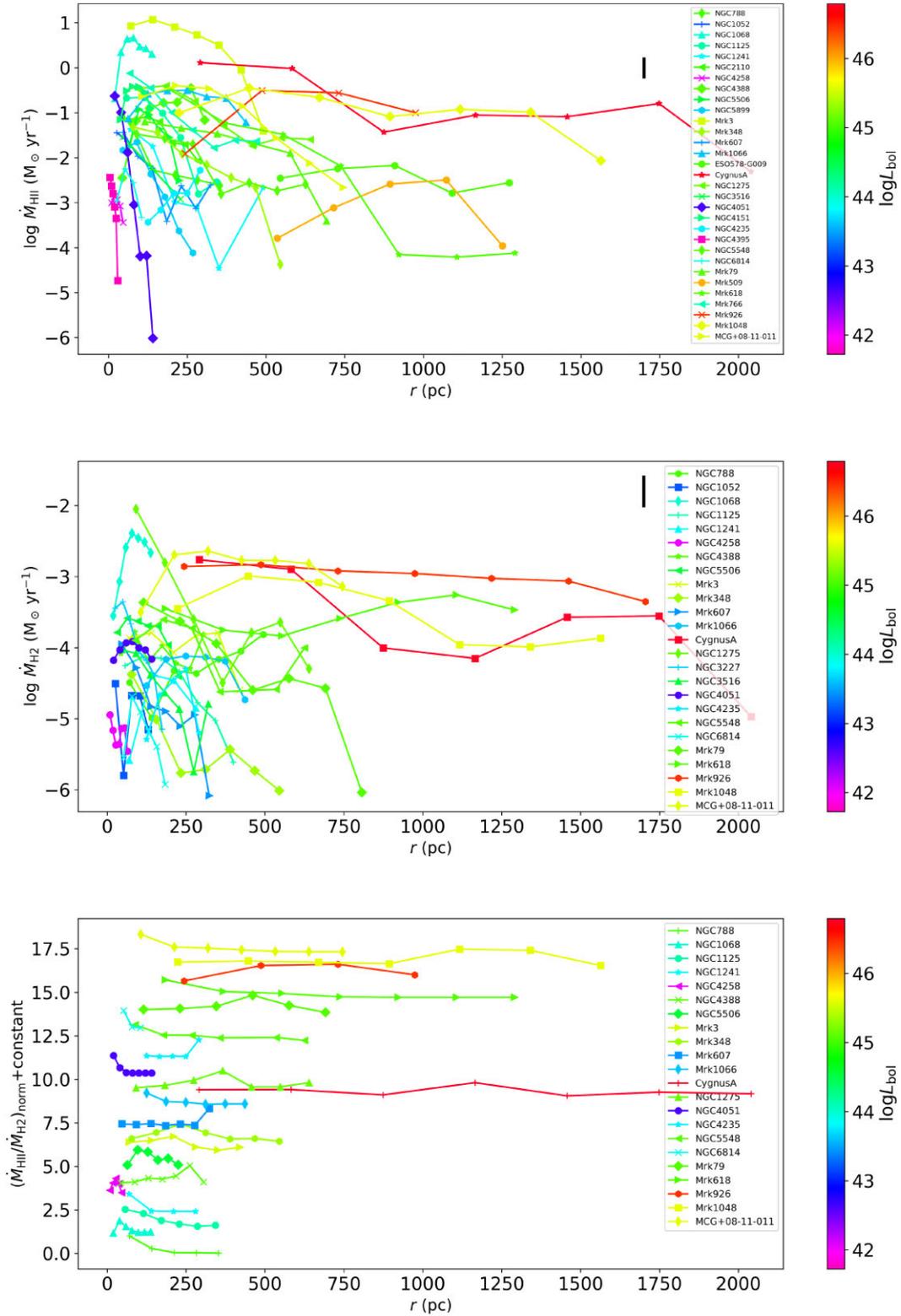
Figure 5. Radial profiles of the mass-outflow rates in ionized (top panel) and hot molecular (middle panel) gas for the galaxies in our sample with detected outflows. The vertical bar in the top-right corner shows typical uncertainties in the mass-outflow rates. The bottom panel shows radial profiles of the normalized ratio between the ionized and molecular outflow rates, plus an arbitrary constant, for objects with outflows in both phases. All profiles are colour coded by the AGN bolometric luminosity, as indicated by the colour bars.
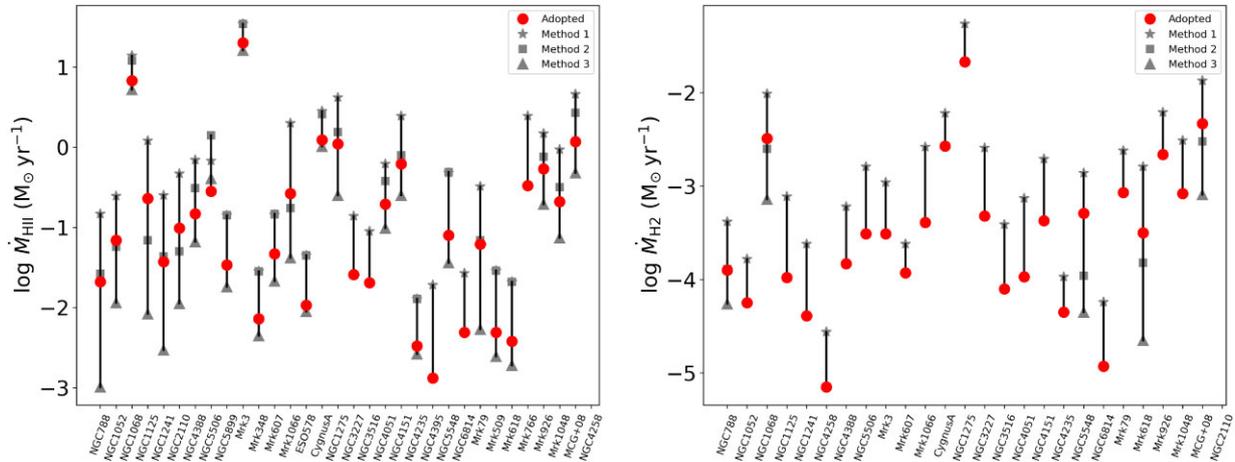
Figure 6. Comparison of the global mass-outflow rates in ionized (left-hand panel) and hot molecular (right-hand panel) gas obtained using different assumptions (see Section 6).

IFS of nearby Seyfert galaxies (Riffel et al. 2009; Müller-Sánchez et al. 2011; Riffel & Storchi-Bergmann 2011a, b; Riffel, Storchi-Bergmann & Winge ; Barbosa et al. 2014; Schnorr-Müller et al. 2014, 2016; Riffel, Storchi-Bergmann & Riffel 2015; Riffel, Hekatelyne & Freitas 2018a; Diniz et al. 2019; Mingozzi et al. 2019; Shimizu et al. 2019; Couto et al. 2020; Avery et al. 2021; Riffel 2021; Bianchin et al. 2022; Kakkad et al. 2022), QSOs at $z \approx 0.3$ (Dall'Agnol de Oliveira et al. 2021), and $z = 2$–3 (Kakkad et al. 2020; Vayner et al. 2021).

The ionized mass-outflow rates estimated for our sample span two orders of magnitude, ranging from 10^{-3} to 10^1 M$_\odot$ yr^{-1}, in agreement with the values available in the literature (Fig. 8). The top-right panel of Fig. 8 shows a plot of the mass-outflow rate in hot molecular gas versus the bolometric luminosity for our sample. Hot molecular gas outflows are scarce in the literature and trace only a small fraction of the molecular gas reservoir in the central region of galaxies (e.g. Dale et al. 2005; Mazzalay et al. 2013). We find outflow rates in the range from 10^{-5} to 10^{-2} M$_\odot$ yr^{-1}, considering estimates using the two methods. These values are consistent with the estimates for the hot molecular gas, available in the literature (e.g. Diniz et al. 2015; Riffel et al. 2020; Bianchin et al. 2022).

The bottom panels of Fig. 8 show plots of the kinetic power of the outflows for the ionized (left-hand panel) and molecular (right-hand panel) gas versus the AGN bolometric luminosity. We include estimates of the kinetic power from the literature, obtained from the same references used to compile the values of mass-outflow rates, described above. The kinetic powers of the ionized outflows in our sample are in the range of $\sim 10^{37}$–10^{43} erg s^{-1}, in good agreement with values from the literature at the same range of bolometric luminosity. The kinetic powers of the hot molecular outflows are on average three orders of magnitude lower than those in ionized gas, with values ranging from 10^{35} to 10^{39} erg s^{-1}.

5. DISCUSSION

In luminous quasars, the gas emission is usually dominated by outflowing gas (e.g. Kakkad et al. 2020; Vayner et al. 2021). Although ionized outflows are also frequently reported in LLAGN, a significant fraction of line emission in the inner kpc arises from gas with motions dominated by the gravitational potential of the galaxy (e.g. Davies et al. 2007; Schönell et al. 2019; Fonseca-Faria et al. 2021; Ruschel-Dutra et al. 2021; Bianchin et al. 2022). We find that 79 per cent of

our sample presents ionized outflows. Recently, Ruschel-Dutra et al. (2021) found outflows in 70 per cent of their sample composed of 30 AGN at $z \le 0.02$ using optical Gemini Multi-Object Spectrograph (GMOS) IFU observations, while Kakkad et al. (2022) studied ionized outflows in a sample of 22 X-ray selected AGN at $z \le 0.1$ observed with the Multi Unit Spectroscopic Explorer (MUSE) instrument at the Very Large Telescope (VLT).

We find that the ionized outflows correspond to a median of 15 per cent of the mass of ionized gas in our sample. As shown in Table 2 and Fig. 7, our sample spans a wide range in fraction of gas in the outflow relative to the total gas mass, which is consistent with previous observations (e.g. Müller-Sánchez et al. 2011; Riffel et al. , 2020; May et al. 2018; Riffel 2021; Bianchin et al. 2022). As shown in Fig. 7, there is a positive trend between the fraction of the gas in the outflow in ionized and molecular gas phases (middle panel), but there is no clear relation between the masses of the gas in the outflow in both phases with the luminosity (right-hand panel).

The fraction of objects with hot molecular outflows in our sample is 76 per cent. The contribution of hot molecular outflows to the total mass of hot molecular gas in the inner region of the observed galaxies is 13 per cent, while if we consider only galaxies with outflows, this contribution slightly increases to 15 per cent. This is consistent with previous observations of nearby active galaxies, which indicate that the hot molecular hydrogen in the inner kpc of nearby AGN hosts is more restricted to the galaxy disc, while the ionized gas usually presents an outflowing component traced by gas that extends to higher latitudes above the disc (e.g. Riffel et al. 2015, 2018b, 2021b; Ramos Almedia et al. 2017; Storchi-Bergmann & Schnorr-Müller 2019; Speranza et al. 2022).

We can compare the properties of the outflows observed in both, hot molecular and ionized gas, phases. Wind scaling relations suggest that the molecular gas phases are relatively more important in lower luminosity objects, but similar to the ionized gas phase in higher luminosity AGN, as indicated by the higher slopes of the correlations of winds properties with the AGN bolometric luminosity observed in ionized gas, relative to those seen in cold molecular gas (Fiore et al. 2017). As shown in Fig. 7, we do not find a clear relation between the ratio of the gas masses of ionized and hot molecular gas with the luminosity. In addition, simulations aimed at investigating outflow properties as a function of radius for different gas phases, indicate that the molecular phase of the outflow is generated from the cooling of the gas trapped into the outflow, and so one would

Table 2. Properties of the ionized gas outflows. (1) Name of the galaxy; (2) Adopted distance: For most galaxies, the distances are estimated from the redshift, except for except for those with accurate distance determinations: NGC 3227 (Tonry et al. 2001), NGC 4051 (Yuan et al. 2020), NGC 4151 (Yuan et al. 2021), NGC 4258 (Reid et al. 2019), NGC 4395 (Thim et al. 2004), and NGC 6814 (Bentz et al. 2019); (3) AGN bolometric luminosity; (4) Radius of the bulk of the outflow (spherical geometry); (5) Radius of the peak of the outflow (spherical shells geometry); (6) Total mass of the outflow considering only spaxels in the KDR; (7) Mass fraction of the gas in the outflow; (8–12) Properties of the outflows estimated using the two methods described in the text.

(1)	(2)	(3)	(4)	(5)	(6)	(7)	(8)	(9) Global/bulk outflow	(10)	(11) Radial profiles	(12)
Galaxy	D (Mpc)	$\log L_{bol}$ (erg s^{-1})	R_{out} (pc)	R_{peak} (pc)	$\log M_{out}$ (M$_\odot$)	f_{out}	V_{out} (km s^{-1})	$\log \dot{M}_{out}^{b}$ (M$_\odot$ yr^{-1})	$\log \dot{E}_{out}^{b}$ (erg s^{-1})	$\log \dot{M}_{peak}$ (M$_\odot$ yr^{-1})	$\log \dot{E}_{peak}$ (erg s^{-1})
Type 2											
NGC788	58.3	45.02	165 ± 39	70 ± 30	3.93 ± 0.49	0.04 ± 0.04	284 ± 49	−1.68 ± 0.50	38.73 ± 0.50	−1.66 ± 0.50	38.82 ± 0.50
NGC1052	21.4	43.23	97 ± 34	25 ± 34	3.54 ± 0.46	0.28 ± 0.25	459 ± 37	−1.16 ± 0.47	39.66 ± 0.47	−1.45 ± 0.52	39.36 ± 0.52
NGC1068	16.3	43.98	414 ± 29	78 ± 24	5.74 ± 0.19	0.50 ± 0.13	922 ± 42	0.83 ± 0.19	42.26 ± 0.19	0.61 ± 0.21	41.97 ± 0.22
NGC1125	47.1	44.15	168 ± 104	114 ± 102	4.83 ± 0.14	0.14 ± 0.07	302 ± 32	−0.64 ± 0.24	39.82 ± 0.24	−0.95 ± 0.33	39.43 ± 0.34
NGC1241	57.9	43.82	149 ± 40	70 ± 31	4.00 ± 0.68	0.12 ± 0.20	371 ± 45	−1.43 ± 0.68	39.21 ± 0.68	−1.51 ± 0.68	39.12 ± 0.68
NGC2110	33.4	44.99	283 ± 41	121 ± 33	4.39 ± 0.32	0.18 ± 0.09	424 ± 37	−1.01 ± 0.32	39.75 ± 0.32	−1.36 ± 0.33	39.32 ± 0.33
NGC4258	7.6	42.03	–	–	–	–	–	–	–	–	–
NGC4388	36.0	45.08	495 ± 80	261 ± 41	4.90 ± 0.28	0.16 ± 0.07	366 ± 39	−0.83 ± 0.29	39.80 ± 0.29	−0.69 ± 0.29	39.76 ± 0.29
NGC5506	26.6	44.57	334 ± 46	96 ± 40	4.70 ± 0.08	0.05 ± 0.01	552 ± 42	−0.55 ± 0.10	40.44 ± 0.10	−0.57 ± 0.17	40.38 ± 0.18
NGC5899	36.9	43.65	153 ± 33	89 ± 29	3.74 ± 0.43	0.16 ± 0.13	381 ± 42	−1.47 ± 0.44	39.19 ± 0.44	−1.65 ± 0.44	39.00 ± 0.44
Mrk3	57.9	45.54	239 ± 31	140 ± 29	6.51 ± 0.15	0.56 ± 0.11	939 ± 48	1.30 ± 0.16	42.74 ± 0.16	1.07 ± 0.17	42.56 ± 0.18
Mrk348	64.3	45.33	346 ± 60	233 ± 40	3.57 ± 0.42	0.02 ± 0.04	474 ± 50	−2.14 ± 0.43	38.71 ± 0.43	−2.15 ± 0.43	38.59 ± 0.43
Mrk607	38.1	43.44	146 ± 35	46 ± 33	3.93 ± 0.18	0.13 ± 0.09	352 ± 53	−1.33 ± 0.20	39.27 ± 0.21	−1.44 ± 0.29	39.13 ± 0.29
Mrk1066	51.4	43.61	365 ± 40	249 ± 33	5.16 ± 0.15	0.11 ± 0.06	374 ± 31	−0.58 ± 0.16	40.06 ± 0.16	−0.85 ± 0.17	39.62 ± 0.17
ESO578–G009	150.0	45.06	576 ± 178	909 ± 78	4.26 ± 0.53	0.04 ± 0.05	564 ± 143	−1.97 ± 0.54	39.03 ± 0.54	−2.17 ± 0.54	38.52 ± 0.54
Cygnus A	240.4	46.80	268 ± 41	291 ± 39	6.19 ± 0.25	0.28 ± 0.10	574 ± 45	0.09 ± 0.25	41.11 ± 0.25	−0.01 ± 0.26	41.28 ± 0.26
Type 1											
NGC1275	75.4	45.14	168 ± 50	91 ± 49	5.52 ± 0.35	0.28 ± 0.16	480 ± 46	0.04 ± 0.36	40.90 ± 0.36	−0.13 ± 0.38	40.67 ± 0.38
NGC3227	20.5	43.66	201 ± 38	49 ± 27	3.47 ± 0.33	0.03 ± 0.05	402 ± 46	−1.59 ± 0.34	39.12 ± 0.34	−1.60 ± 0.36	39.09 ± 0.36
NGC3516	37.7	44.56	67 ± 35	45 ± 35	3.21 ± 0.76	0.21 ± 0.20	381 ± 46	−1.69 ± 0.76	38.97 ± 0.76	−1.89 ± 0.76	38.78 ± 0.76
NGC4051	16.6	42.62	109 ± 43	20 ± 40	4.04 ± 0.81	0.17 ± 0.20	371 ± 50	−0.71 ± 0.42	39.93 ± 0.31	−0.90 ± 0.37	39.77 ± 0.28
NGC4151	15.8	44.32	393 ± 44	76 ± 39	5.00 ± 0.17	0.28 ± 0.06	430 ± 30	−0.21 ± 0.18	40.56 ± 0.18	−0.48 ± 0.24	40.21 ± 0.24
NGC4235	34.3	43.77	603 ± 84	290 ± 30	3.21 ± 0.65	0.17 ± 0.28	472 ± 80	−2.48 ± 0.65	38.37 ± 0.65	−2.21 ± 0.65	38.55 ± 0.65
NGC4395	4.0	41.72	195 ± 48	4 ± 44	1.70 ± 0.40	0.07 ± 0.05	233 ± 31	−2.88 ± 0.41	37.36 ± 0.41	−3.15 ± 1.02	36.89 ± 1.02
NGC5548	73.7	45.08	215 ± 49	89 ± 45	4.57 ± 1.13	0.11 ± 0.20	383 ± 37	−1.10 ± 1.13	39.56 ± 1.13	−1.32 ± 1.13	39.36 ± 1.13
NGC6814	21.6	43.90	188 ± 44	52 ± 40	2.78 ± 0.64	0.09 ± 0.14	364 ± 44	−2.31 ± 0.64	38.31 ± 0.64	−2.38 ± 0.65	38.24 ± 0.65
Mrk79	95.1	45.08	205 ± 58	115 ± 55	4.59 ± 0.50	0.13 ± 0.13	347 ± 38	−1.21 ± 0.50	39.37 ± 0.50	−1.43 ± 0.51	39.14 ± 0.51
Mrk509	147.4	46.00	505 ± 67	1072 ± 31	4.10 ± 0.68	0.01 ± 0.06	318 ± 50	−2.31 ± 0.68	38.19 ± 0.68	−2.22 ± 0.68	38.05 ± 0.68
Mrk618	152.1	45.06	336 ± 68	553 ± 40	3.78 ± 0.77	0.00 ± 0.02	354 ± 58	−2.42 ± 0.77	38.18 ± 0.77	−2.15 ± 0.77	38.47 ± 0.77
Mrk766	55.3	44.08	222 ± 57	67 ± 42	5.11 ± 0.44	0.15 ± 0.13	359 ± 44	−0.48 ± 0.44	40.13 ± 0.44	−0.49 ± 0.46	40.15 ± 0.46
Mrk926	201.0	46.45	225 ± 42	487 ± 38	5.73 ± 0.39	0.21 ± 0.14	493 ± 38	−0.27 ± 0.39	40.61 ± 0.39	−0.42 ± 0.39	40.42 ± 0.39
Mrk1044	70.7	44.01	–	–	–	–	–	–	–	–	–
Mrk1048	184.3	45.62	287 ± 56	446 ± 48	5.51 ± 0.47	0.21 ± 0.19	374 ± 39	−0.68 ± 0.47	39.96 ± 0.47	−0.90 ± 0.47	39.64 ± 0.47
MCG + 08-11-011	87.9	45.59	206 ± 45	212 ± 43	5.73 ± 0.42	0.25 ± 0.19	439 ± 36	0.07 ± 0.42	40.86 ± 0.43	−0.26 ± 0.43	40.45 ± 0.43

Table 3. Properties of the molecular outflows. (1) Name of the galaxy; (2) Adopted distance: For most galaxies, the distances are estimated from the redshift, except for except for those with accurate distance determinations: NGC 3227 (Tonry et al. 2001), NGC 4051 (Yuan et al. 2021), NGC 4151 (Yuan et al. 2020), NGC 4258 (Reid et al. 2019), NGC 4395 (Thim et al. 2004), and NGC 6814 (Bentz et al. 2019); (3) AGN bolometric luminosity; (4) Radius of the bulk of the outflow (spherical geometry); (5) Radius of the peak of the outflow (spherical shells geometry); (6) Total mass of the outflow considering only spaxels in the KDR; (7) Mass fraction of the gas in the outflow; (8–12) Properties of the outflows estimated using the two methods described in the text.

| (1)	(2)	(3)	(4)	(5)	(6)	(7)	(8)	(9) Global/bulk outflow	(10)	(11) Radial profiles	(12)
Galaxy	D (Mpc)	$\log L_{bol}$ (erg s^{-1})	R_{out} (pc)	R_{peak} (pc)	$\log M_{out}$ (M$_\odot$)	f_{out}	V_{out} (km s^{-1})	$\log \dot{M}_{out}^{b}$ (M$_\odot$ yr^{-1})	$\log \dot{E}_{out}^{b}$ (erg s^{-1})	$\log \dot{M}_{peak}$ (M$_\odot$ yr^{-1})	$\log \dot{E}_{peak}$ (erg s^{-1})
Type 2											
NGC788	58.3	45.02	557 ± 54	494 ± 29	1.95 ± 0.42	0.15 ± 0.11	516 ± 47	−3.90 ± 0.42	37.02 ± 0.42	−3.88 ± 0.43	37.03 ± 0.43
NGC1052	21.4	43.23	257 ± 41	25 ± 36	0.92 ± 0.39	0.07 ± 0.05	408 ± 44	−4.25 ± 0.40	36.47 ± 0.40	−4.37 ± 0.49	36.31 ± 0.49
NGC1068	16.3	43.98	530 ± 29	78 ± 24	2.92 ± 0.08	0.29 ± 0.08	375 ± 27	−2.49 ± 0.08	38.16 ± 0.09	−2.56 ± 0.14	38.18 ± 0.15
NGC1125	47.1	44.15	251 ± 104	114 ± 102	1.65 ± 0.32	0.11 ± 0.05	309 ± 28	−3.98 ± 0.33	36.50 ± 0.33	−4.29 ± 0.39	36.16 ± 0.39
NGC1241	57.9	43.82	230 ± 33	140 ± 31	1.28 ± 0.32	0.04 ± 0.06	317 ± 30	−4.39 ± 0.32	36.11 ± 0.32	−4.56 ± 0.34	35.91 ± 0.34
NGC2110	33.4	44.99	–	–	–	–	–	–	–	–	–
NGC4258	7.6	42.03	412 ± 73	–	−0.22 ± 0.31	0.06 ± 0.09	418 ± 54	−5.15 ± 0.32	35.59 ± 0.32	−5.07 ± 0.39	35.54 ± 0.39
NGC4388	36.0	45.08	419 ± 77	305 ± 42	1.87 ± 0.23	0.06 ± 0.06	332 ± 45	−3.83 ± 0.24	36.71 ± 0.25	−3.93 ± 0.25	36.49 ± 0.25
NGC5506	26.6	44.57	291 ± 43	64 ± 39	1.92 ± 0.14	0.12 ± 0.07	318 ± 28	−3.51 ± 0.16	36.99 ± 0.16	−3.73 ± 0.21	36.76 ± 0.21
NGC5899	36.9	43.65	–	–	–	–	–	–	–	–	–
Mrk3	57.9	45.54	294 ± 40	350 ± 30	2.21 ± 0.30	0.16 ± 0.08	363 ± 31	−3.51 ± 0.30	37.11 ± 0.30	−3.79 ± 0.31	36.86 ± 0.31
Mrk348	64.3	45.33	–	–	–	–	–	–	–	–	–
Mrk607	38.1	43.44	178 ± 36	46 ± 32	1.44 ± 0.17	0.22 ± 0.05	333 ± 40	−3.93 ± 0.18	36.61 ± 0.19	−4.01 ± 0.27	36.56 ± 0.28
Mrk1066	51.4	43.61	361 ± 37	186 ± 33	2.53 ± 0.11	0.15 ± 0.06	243 ± 26	−3.39 ± 0.12	36.88 ± 0.13	−3.59 ± 0.13	36.61 ± 0.14
ESO578–G009	150.0	45.06	–	–	–	–	–	–	–	–	–
CygnusA	240.4	46.80	218 ± 42	291 ± 39	3.48 ± 0.14	0.14 ± 0.07	527 ± 44	−2.57 ± 0.15	38.38 ± 0.16	−2.70 ± 0.16	38.33 ± 0.17
Type 1											
NGC1275	75.4	45.14	165 ± 51	91 ± 49	3.88 ± 0.12	0.33 ± 0.05	402 ± 45	−1.67 ± 0.16	39.04 ± 0.17	−1.81 ± 0.23	38.94 ± 0.24
NGC3227	20.5	43.66	210 ± 29	49 ± 27	1.85 ± 0.13	0.09 ± 0.04	330 ± 32	−3.32 ± 0.14	37.22 ± 0.15	−3.56 ± 0.23	36.99 ± 0.23
NGC3516	37.7	44.56	255 ± 49	45 ± 34	1.40 ± 0.30	0.15 ± 0.07	336 ± 35	−4.10 ± 0.30	36.45 ± 0.30	−4.27 ± 0.35	36.30 ± 0.35
NGC4051	16.6	42.62	404 ± 42	80 ± 39	1.46 ± 0.13	0.14 ± 0.07	278 ± 25	−3.97 ± 0.14	36.42 ± 0.14	−4.29 ± 0.48	36.07 ± 0.48
NGC4151	15.8	44.32	396 ± 42	76 ± 39	1.98 ± 0.17	0.20 ± 0.05	310 ± 25	−3.37 ± 0.17	37.12 ± 0.18	−3.66 ± 0.23	36.70 ± 0.24
NGC4235	34.3	43.77	512 ± 45	249 ± 29	1.25 ± 0.23	0.13 ± 0.04	492 ± 36	−4.35 ± 0.23	36.54 ± 0.23	−4.15 ± 0.24	36.71 ± 0.24
NGC4395	4.0	41.72	–	–	–	–	–	–	–	–	–
NGC5548	73.7	45.08	229 ± 48	178 ± 44	2.33 ± 0.69	0.27 ± 0.25	445 ± 31	−3.29 ± 0.69	37.51 ± 0.69	−3.48 ± 0.70	37.19 ± 0.70
NGC6814	21.6	43.90	500 ± 77	78 ± 38	0.68 ± 0.40	0.06 ± 0.04	289 ± 38	−4.93 ± 0.40	35.49 ± 0.40	−4.99 ± 0.43	35.34 ± 0.43
Mrk79	95.1	45.08	164 ± 56	115 ± 55	2.58 ± 0.19	0.19 ± 0.05	398 ± 39	−3.07 ± 0.22	37.63 ± 0.22	−3.25 ± 0.26	37.44 ± 0.26
Mrk509	147.4	46.00	–	–	–	–	–	–	–	–	–
Mrk618	152.1	45.06	404 ± 44	922 ± 39	2.81 ± 0.34	0.13 ± 0.07	335 ± 28	−3.50 ± 0.34	37.05 ± 0.34	−3.61 ± 0.34	37.01 ± 0.35
Mrk766	55.3	44.08	–	–	–	–	–	–	–	–	–
Mrk926	201.0	46.45	313 ± 41	487 ± 38	3.64 ± 0.23	0.32 ± 0.10	354 ± 29	−2.66 ± 0.23	37.94 ± 0.23	−2.94 ± 0.23	37.74 ± 0.23
Mrk1044	70.7	44.01	–	–	–	–	–	–	–	–	–
Mrk1048	184.3	45.62	299 ± 51	446 ± 48	3.21 ± 0.19	0.26 ± 0.07	316 ± 28	−3.08 ± 0.20	37.42 ± 0.20	−3.23 ± 0.20	37.32 ± 0.20
MCG + 08-11-011	87.9	45.59	366 ± 47	425 ± 42	3.58 ± 0.20	0.35 ± 0.10	439 ± 28	−2.33 ± 0.20	38.45 ± 0.21	−2.60 ± 0.21	38.11 ± 0.22
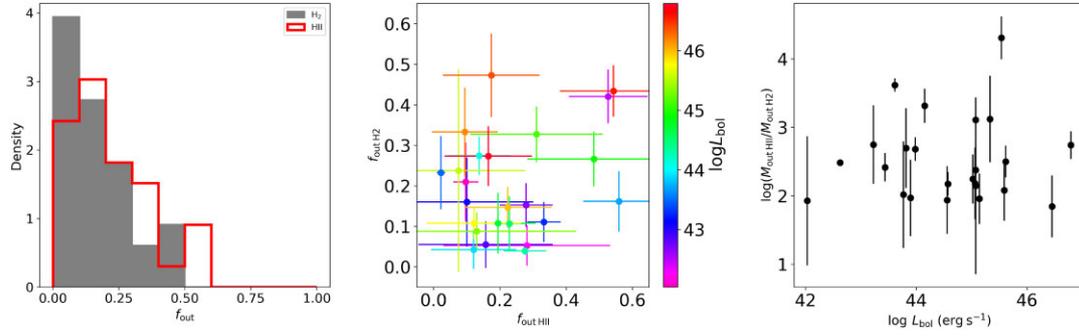
Figure 7. Left-hand panel: Distribution of the fraction of gas in the outflow ($f_{out} = \frac{M_{out}}{M_{total}}$), compared to the total masses of ionized (in red) and molecular (in grey) gas. Middle panel: Plot of the f_{out} observed in H_2 (y-axis) versus those seen in H II (x-axis), colour coded by the AGN bolometric luminosity. Right-hand panel: Plot of the ratio of mass of ionized and molecular gas in the outflow versus the AGN bolometric luminosity.
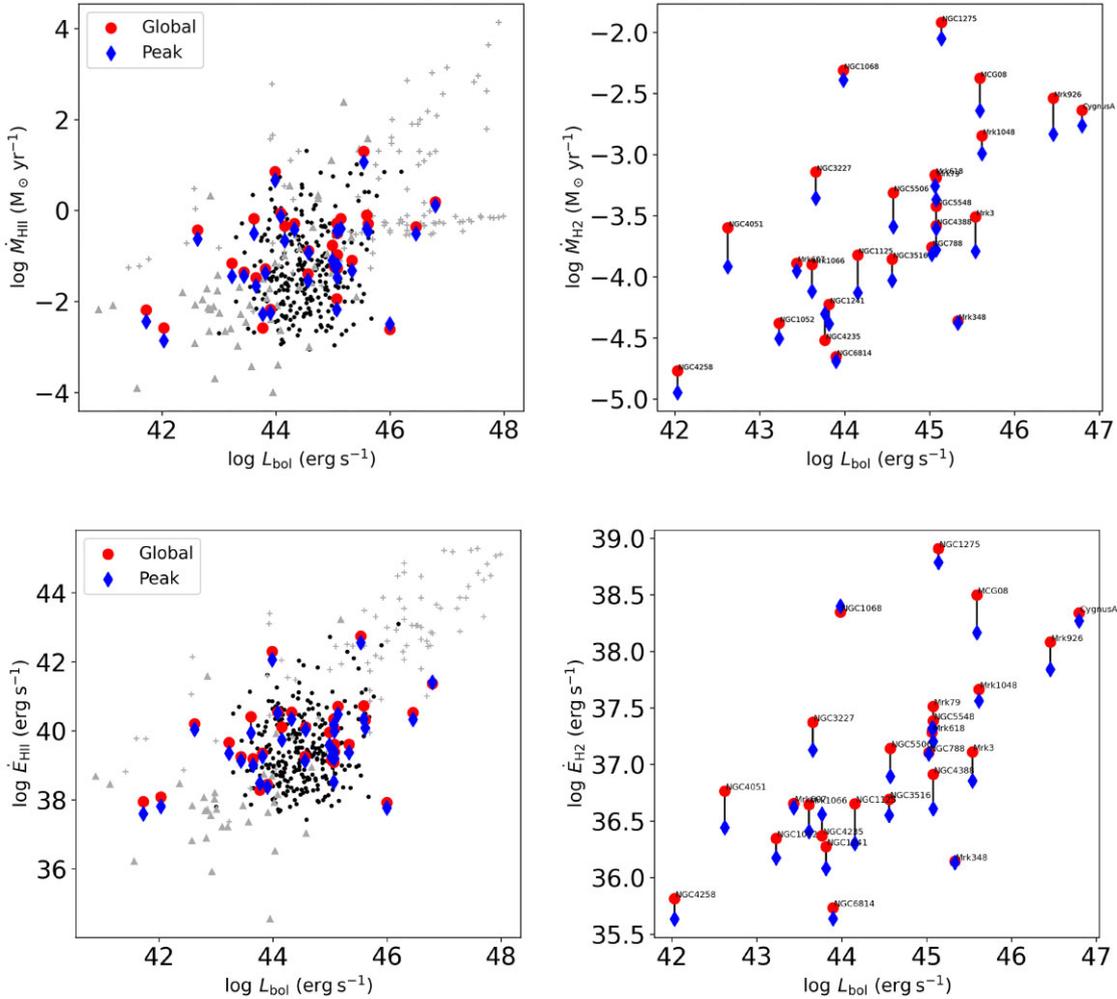

Figure 8. Top panels: Plot of mass-outflow rates versus AGN bolometric luminosity. Mass-outflow rates for the ionized (left-hand panel) and hot molecular gas (right-hand panel) obtained by assuming a spherical shell geometry (red circles) and peak from radial profiles (blue diamonds) are shown for each object. The grey and black points are a compilation of values from the literature, as described in the text. Bottom panels: Same as top panels, but for the kinetic power of the outflows. Typical uncertainties in both parameters are 0.2 dex for both gas phases, as shown in Tables 2 and 3.

expect that the molecular phase is more important at larger radii, relative to the ionized phase (e.g. Ferrara & Scannapieco 2016; Costa et al. 2018; Richings & Faucher-Giguère 2018; Richings, Faucher-Giguère & Stern 2021). As shown in the bottom panel of Fig. 5, we do not find a clear relation between the mass-outflow rates in

ionized and hot molecular gas with the distance from the centre. A possible explanation for the absence of relations between the relative outflow properties in both phases with the luminosity and radius, is that the hot molecular gas phase observed via the H_2 emission lines represents only the heated surface of a much larger colder molecular

gas reservoir (Dale et al. 2005; Mazzalay et al. 2013), considered in the simulations.

The mass-outflow rates and kinetic powers of the outflows estimated for our sample are in agreement with previous measurements for AGN of similar luminosity. However, as can be seen in Fig. 8, the scatters of the relations of log $\dot{M}_{out}$ versus log L_{bol} and log $\dot{E}_{out}$ versus log L_{bol} are high, if we consider all measurements available in the literature and used for comparison here. The density of the outflow is a function of the radius, as well as the ionized gas density at a given radius is a function of the AGN luminosity (Davies et al. 2020; Revalski et al. 2022), and thus the use of a fixed density value to estimate the mass-outflow rate may reduce the scatter of the correlation between log $\dot{M}_{out}$ and log L_{bol}. In the luminosity range of our sample, the mass-outflow rates in ionized gas cover four orders of magnitude, while the kinetic powers spans three orders of magnitude. The wide ranges of values observed for log $\dot{M}_{out}$ and log $\dot{E}_{out}$ are in good agreement with previous works and are partially due to the assumptions made to calculate the outflow properties by distinct works, which include assumptions on the electron density estimates, geometry, and velocity of the outflows (see Davies et al. 2020, for a detailed discussion). An important caveat is that outflow rates are defined as the amount of material passing through a common radius, so they may be estimated globally for the entire outflow, or outflow rates measured from individual spaxels, may be added azimuthally to produce radial outflow rate profiles (see Fig. 5 and Revalski et al. 2021). However, outflow rates cannot be added radially. These instantaneous outflow rates are directly related to the spatial resolution of the data, such that higher spatial sampling yields larger instantaneous rates, because they account for material passing through multiple boundaries for a fixed evacuation time (Veilleux et al. 2017; Kakkad et al. 2022). This can explain why mass-outflow rates and kinetic powers estimated by radially summing the individual spaxels are systematically larger by up to two orders of magnitude as compared to the global and radial estimates (e.g. Kakkad et al. 2022).

We can compare the kinetic coupling efficiencies ($\dot{E}_K/L_{bol}$) for observed ionized outflows in our sample with theoretical predictions. For AGN feedback to become efficient in suppressing star formation, the models require a minimum coupling efficiency (ε_f) in the range of 0.5–20 per cent (Di Matteo et al. 2005; Hopkins & Elvis 2010; Dubois et al. 2014; Schaye et al. 2015; Weinberger et al. 2017). However, as discussed in Harrison et al. (2018), it is unlikely that all the injected energy becomes kinetic power in the outflow and a direct comparison between observed $\dot{E}_K/L_{bol}$ and predicted ε_f is not straightforward. Indeed, recent numerical simulations indicate that the kinetic energy of the outflows represents <20 per cent of the total emitted outflow energy (Richings & Faucher-Giguère 2018).

With the above caveat in mind, we estimate the kinetic coupling efficiencies for the ionized gas in our sample. We find that none object in our sample present outflows with kinetic powers corresponding to >0.5 per cent of the AGN bolometric luminosity. The median value of the kinetic coupling efficiency using the global kinetic power of the ionized outflows is $\dot{E}_K/L_{bol} \approx 1.8 \times 10^{-3}$. The kinetic powers of the hot molecular outflows are about 2 orders of magnitude lower than those of the ionized gas, and thus they are also not powerful enough to suppress star formation in the galaxies. However, besides the fact that $\dot{E}_K/L_{bol} < \varepsilon_f$ aforementioned, the outflows in AGN are seen in multiple gas phases and the kinetic power of dense cold molecular outflows are expected to be larger. Thus, even if the ionized outflows seen here are not powerful enough to suppress star formation in the host galaxies, we cannot discard AGN feedback as an important mechanism in shaping the evolution of the galaxies in our sample.
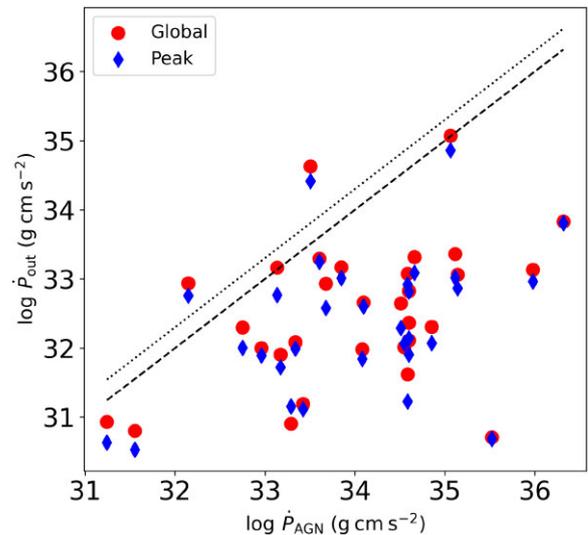

Figure 9. Momentum flux of the ionized outflows versus the AGN photon momentum flux for our sample. Red circles represent estimates obtained by assuming a spherical shell geometry and blue diamonds represent peak estimates from radial profiles. The dotted and dashed lines correspond to constant ratios of 2:1 and 1:1, respectively, useful to investigate the origin of the outflows.

In order to investigate the physical mechanism that drives the outflows observed in our sample, we compute the momentum flux of the outflow by $\dot{P}_{out} = \dot{M} \times v_{out}$, where v_{out} is the velocity of the outflow. In Fig. 9, we present a plot of $\dot{P}_{out}$ versus the photon momentum flux ($\dot{P}_{AGN} = L_{AGN}/c$, where L_{AGN} is the AGN bolometric luminosity), which can yield insights into the origin of winds (Murray et al. 2005; Thompson et al. 2015; Costa et al. 2018; Veilleux et al. 2020; Vayner et al. 2021). To estimate $\dot{P}_{out}$, we use the same definition for the velocity of the outflow previously used to calculate the mass-outflow rates. The dotted and dashed lines show a 2:1 and 1:1 constant relations, respectively, that can be used to investigate the driving mechanism of the outflows. Theoretical studies suggest that $\dot{P}_{out} \gtrsim 2\dot{P}_{AGN}$ on scales $\lesssim$1 kpc are due to radiation pressure-driven winds in a high-density, optically thick environment, where far-infrared photons are scattered multiple times (Thompson et al. 2015; Costa et al. 2018). Values of $\dot{P}_{out} \lesssim 1\dot{P}_{AGN}$ are usually attributed to radiation-pressure driven winds in low-density environments or shocked AGN winds (Faucher-Giguère & Quataert 2012). Most objects in our sample are below the 1:1 line in Fig. 9, indicating that the winds are driven by radiation pressure in low-density environment, with possible contribution from shocks as suggested also in our previous studies (e.g. Riffel et al. 2021a, b).

6. CONCLUSIONS

We have studied the molecular and ionized gas kinematics of the inner 0.04–2 kpc of a sample of 33 AGN hosts with $0.001 \lesssim z \lesssim 0.056$ and hard X-ray luminosities of $41 \lesssim \log L_X/(\text{erg s}^{-1}) \lesssim 45$. The K-band observations were performed with the Gemini NIFS instrument, with a field of view covering from the inner 75×75 pc^2 to 3.6×3.6 kpc^2 at spatial resolutions of 6–250 pc and velocity resolution of $\sigma_{inst} \sim 20$ km s^{-1}. We use the W_{80}, V_{peak}, and V_{cen} parameters for the H$_2$ 2.1218 μm and Br γ emission lines to identify regions where the gas motions are dominated by kinematic disturbances due to the AGN and regions where the gas motions are due the gravitational potential of galaxies. Our main conclusions are as follows:

(i) We identify ionized gas KDRs in 31 galaxies (94 per cent) of our sample, while 25 objects (76 per cent) present KDRs in molecular gas.

(ii) We attribute the KDR as being produced by AGN outflows and estimate their mass-outflow rates and kinetic powers in two ways: (a) by assuming an spherical geometry, resulting in *global outflow* properties and (b) adopting the *peak* outflow properties, derived from their radial profiles.

(iii) The masses of the outflowing gas are in the ranges of 10^2–10^7 and 10^0–10^4 M$_\odot$ for the ionized and hot molecular gas, respectively. These values correspond to median fractions of the gas in the outflow relative to the total amount of gas of about 15 per cent for both ionized and hot molecular gas (within a typical covered region of a few 100-pc radius at the galaxies).

(iv) The mass-outflow rates in ionized gas are in the range of 10^{-3}–10^1 M$_\odot$ yr^{-1}. The kinetic powers of the ionized outflows are in the range of $\sim 10^{37}$–10^{43} erg s^{-1}, being <0.5 per cent of the AGN bolometric luminosity for most objects, with a median kinetic coupling efficiency in our sample is $\dot{E}_K/L_{bol} \approx 1.8 \times 10^{-3}$. The estimated mass-outflow rates and kinetic powers of the outflows are consistent with previous estimates for objects in the same luminosity range, but a large scatter of the wind scaling relations is seen in the lower luminosity range.

(v) The mass-outflow rates in molecular gas range from 10^{-5} to 10^{-2} M$_\odot$ yr^{-1}, and the kinetic power of the outflows are in the range of 10^{35}–10^{39} erg s^{-1}. Both mass-outflow rates and powers present positive correlations with the AGN bolometric luminosity.

(vi) The momentum flux of the ionized outflows are lower than the photon momentum flux of the accretion disc in most objects, indicating that the observed outflows are consistent with radiation-pressure driven winds in low-density environments including possible contribution of shocked AGN winds.

In summary, our results support the presence of kinematic disturbances produced by the AGN in most sources, with a higher impact in the galaxy produced by the ionized gas outflows as compared to that of the hot molecular gas. This can be attributed mostly to the small mass in this latter gas phase, but its kinematics is also dominated by lower velocities than observed in the ionized gas. Observations in cold molecular gas should be made to investigate the presence of outflows in this gas phase.

DATA AVAILABILITY

The data used in this paper are available in the Gemini Science Archive at: https://archive.gemini.edu/searchform. Processed data cubes used will be shared on reasonable request to the corresponding author.

REFERENCES

Avery C. R. et al., 2021, MNRAS, 503, 5134
Barbosa F. K. B., Storchi-Bergmann T., McGregor P., Vale T. B., Rogemar Riffel A., 2014, MNRAS, 445, 2353
Baron D., Netzer H., 2019, MNRAS, 486, 4290
Bentz M. C., Ferrarese L., Onken C. A., Peterson B. M., Valluri M., 2019, ApJ, 885, 161
Bianchin M. et al., 2022, MNRAS, 510, 639
Brum C., Riffel R. A., Storchi-Bergmann T., Robinson A., Schnorr Müller A., Lena D., 2017, MNRAS, 469, 3405
Burtscher L. et al., 2015, A&A, 578, A47
Burtscher L. et al., 2021, A&A, 654, A132
Caglar T. et al., 2020, A&A, 634, A114
Cappellari M., 2017, MNRAS, 466, 798
Cappellari M., Emsellem E., 2004, PASP, 116, 138
Ciotti L., Ostriker J. P., Proga D., 2010, ApJ, 717, 708
Costa T., Rosdahl J., Sijacki D., Haehnelt M. G., 2018, MNRAS, 479, 2079
Couto G. S., Storchi-Bergmann T., Siemiginowska A., Riffel R. A., Morganti R., 2020, MNRAS, 497, 5103
Dale D. A., Sheth K., Helou G., Regan M. W., Hüttemeister S., 2005, AJ, 129, 2197
Dall'Agnol de Oliveira B. et al., 2021, MNRAS, 504, 3890
Davies R. et al., 2020, MNRAS, 498, 4150
Davies R. I., Müller Sánchez F., Genzel R., Tacconi L. J., Hicks E. K. S., Friedrich S., Sternberg A., 2007, ApJ, 671, 1388
Deconto-Machado A. et al., 2022, A&A, 659, A131
den Brok J. S. et al., 2022, ApJS, 261, 7
Di Matteo T., Springel V., Hernquist L., 2005, Nature, 433, 604
Diniz M. R., Riffel R. A., Riffel R., Crenshaw D. M., Storchi-Bergmann T., Fischer T. C., Schmitt H. R., Kraemer S. B., 2017, MNRAS, 469, 3286
Diniz M. R., Riffel R. A., Storchi-Bergmann T., Riffel R., 2019, MNRAS, 487, 3958
Diniz M. R., Riffel R. A., Storchi-Bergmann T., Winge C., 2015, MNRAS, 453, 1727
Dors O. L., Cardaci M. V., Hägele G. F., Krabbe Â. C., 2014, MNRAS, 443, 1291
Dors O. L., Maiolino R., Cardaci M. V., Hägele G. F., Krabbe A. C., Pérez-Montero E., Armah M., 2020, MNRAS, 496, 3209
Dubois Y. et al., 2014, MNRAS, 444, 1453
Elvis M., 2000, ApJ, 545, 63
Faucher-Giguère C.-A., Quataert E., 2012, MNRAS, 425, 605
Ferrara A., Scannapieco E., 2016, ApJ, 833, 46
Ferrarese L., Merritt D., 2000, ApJ, 539, L9
Fiore F. et al., 2017, A&A, 601, A143
Fischer T. C. et al., 2018, ApJ, 856, 102
Fischer T. C. et al., 2019, ApJ, 875, 102
Fonseca-Faria M. A., Rodríguez-Ardila A., Contini M., Reynaldi V., 2021, MNRAS, 506, 3831
Förster Schreiber N. M. et al., 2019, ApJ, 875, 21

Frank J., King A., Raine D. J., 2002, Accretion Power in Astrophysics: Third Edition. Cambridge Univ. Press, Cambridge

Freitas I. C. et al., 2018, MNRAS, 476, 2760

Gebhardt K. et al., 2000, ApJ, 539, L13

Gültekin K. et al., 2009, ApJ, 698, 198

Harrison C. M., 2017, Nature Astron., 1, 0165

Harrison C. M., Costa T., Tadhunter C. N., Flütsch A., Kakkad D., Perna M., Vietri G., 2018, Nature Astron., 2, 198

Heckman T. M., Kauffmann G., 2011, Science, 333, 182

Hicks E. K. S., Davies R. I., Maciejewski W., Emsellem E., Malkan M. A., Dumas G., Müller-Sánchez F., Rivers A., 2013, ApJ, 768, 107

Hopkins P. F., Elvis M., 2010, MNRAS, 401, 7

Ichikawa K., Ricci C., Ueda Y., Matsuoka K., Toba Y., Kawamuro T., Trakhtenbrot B., Koss M. J., 2017, ApJ, 835, 74

Ilha G. d. S., Bianchin M., Riffel R. A., 2016, Ap&SS, 361, 178

Ilha G. S. et al., 2019, MNRAS, 484, 252

Kakkad D. et al., 2018, A&A, 618, A6

Kakkad D. et al., 2020, A&A, 642, A147

Kakkad D. et al., 2022, MNRAS, 511, 2105

Kormendy J., Ho L. C., 2013, ARA&A, 51, 511

Kovačević-Dojčinović J., Dojčinović I., Lakićević M., Popović L. Č., 2022, A&A, 659, A130

Lamperti I. et al., 2017, MNRAS, 467, 540

Lamperti I. et al., 2021, A&A, 654, A90

Liu G., Zakamska N. L., Greene J. E., Nesvadba N. P. H., Liu X., 2013, MNRAS, 436, 2576

Luo R. et al., 2021, ApJ, 908, 221

Lutz D. et al., 2020, A&A, 633, A134

Magorrian J. et al., 1998, AJ, 115, 2285

Mallmann N. D. et al., 2018, MNRAS, 478, 5491

May D., Rodríguez-Ardila A., Prieto M. A., Fernández-Ontiveros J. A., Diaz Y., Mazzalay X., 2018, MNRAS, 481, L105

Mazzalay X. et al., 2013, MNRAS, 428, 2389

Mazzalay X. et al., 2014, MNRAS, 438, 2036

McElroy R., Croom S. M., Pracy M., Sharp R., Ho I. T., Medling A. M., 2015, MNRAS, 446, 2186

McGregor P. J. et al., 2003, Proc. SPIE Conf. Ser. Vol. 4841, Instrument Design and Performance for Optical/Infrared Ground-based Telescopes. SPIE, Bellingham, p. 1581

Mingozzi M. et al., 2019, A&A, 622, A146

Müller-Sánchez F., Nevin R., Comerford J. M., Davies R. I., Privon G. C., Treister E., 2018, Nature, 556, 345

Müller-Sánchez F., Prieto M. A., Hicks E. K. S., Vives-Arias H., Davies R. I., Malkan M., Tacconi L. J., Genzel R., 2011, ApJ, 739, 69

Murray N., Quataert E., Thompson T. A., 2005, ApJ, 618, 569

Oh K. et al., 2018, ApJS, 235, 4

Osterbrock D. E., Ferland G. J., 2006, Astrophysics of Gaseous Nebulae and Active Galactic Nuclei, 2nd edn. University Science Books, Mill Valley, CA

Penny S. J. et al., 2018, MNRAS, 476, 979

Perna M., Lanzuisi G., Brusa M., Cresci G., Mignoli M., 2017, A&A, 606, A96

Perrotta S., Hamann F., Zakamska N. L., Alexandroff R. M., Rupke D., Wylezalek D., 2019, MNRAS, 488, 4126

Ramos Almedia C., Piqueras López J. Villar-Martín M. Bessiere P. S. 2017, MNRAS, 470, 964

Ramos Almeida C., Acosta-Pulido J. A., Tadhunter C. N., González-Fernández C., Cicone C., Fernández-Torreiro M., 2019, MNRAS, 487, L18

Reid M. J., Pesce D. W., Riess A. G., 2019, ApJ, 886, L27

Revalski M. et al., 2021, ApJ, 910, 139

Revalski M. et al., 2022, ApJ, 930, 14

Ricci C. et al., 2017, ApJS, 233, 17

Richings A. J., Faucher-Giguère C.-A., 2018, MNRAS, 478, 3100

Richings A. J., Faucher-Giguère C.-A., Stern J., 2021, MNRAS, 503, 1568

Riffel R. A. et al., 2018b, MNRAS, 474, 1373

Riffel R. A. et al., 2021b, MNRAS, 504, 3265

Riffel R. A., 2021, MNRAS, 506, 2950

Riffel R. A., Bianchin M., Riffel R., Storchi-Bergmann T., Schönell A. J., Dahmer-Hahn L. G., Dametto N. Z., Diniz M. R., 2021a, MNRAS, 503, 5161

Riffel R. A., Hekatelyne C., Freitas I. C., 2018a, Publ. Astron. Soc. Aust., 35, e040

Riffel R. A., Storchi-Bergmann T., 2011a, MNRAS, 411, 469

Riffel R. A., Storchi-Bergmann T., 2011b, MNRAS, 417, 2752

Riffel R. A., Storchi-Bergmann T., Dors O. L., Winge C., 2009, MNRAS, 393, 783

Riffel R. A., Storchi-Bergmann T., Riffel R., 2015, MNRAS, 451, 3587

Riffel R. A., Storchi-Bergmann T., Riffel R., Dahmer-Hahn L. G., Diniz M. R., Schönell A. J., Dametto N. Z., 2017, MNRAS, 470, 992

Riffel R. A., Storchi-Bergmann T., Riffel R., Pastoriza M. G., 2010, ApJ, 713, 469

Riffel R. A., Storchi-Bergmann T., Winge C., 2013, MNRAS, 430, 2249

Riffel R. A., Storchi-Bergmann T., Zakamska N. L., Riffel R., 2020, MNRAS, 496, 4857

Riffel R. A., Vale T. B., Storchi-Bergmann T., McGregor P. J., 2014, MNRAS, 442, 656

Riffel R. et al., 2022, MNRAS, 512, 3906

Riffel R., Riffel R. A., Ferrari F., Storchi-Bergmann T., 2011, MNRAS, 416, 493

Riffel R., Rodríguez-Ardila A., Pastoriza M. G., 2006, A&A, 457, 61

Rodríguez-Ardila A., Pastoriza M. G., Viegas S., Sigut T. A. A., Pradhan A. K., 2004, A&A, 425, 457

Ruschel-Dutra D. et al., 2021, MNRAS, 507, 74

Ruschel-Dutra D., 2020, danielrd6/ifscube v1.0. Zenodo

Santoro F., Rose M., Morganti R., Tadhunter C., Oosterloo T. A., Holt J., 2018, A&A, 617, A139

Santoro F., Tadhunter C., Baron D., Morganti R., Holt J., 2020, A&A, 644, A54

Schaye J. et al., 2015, MNRAS, 446, 521

Schnorr-Müller A., Storchi-Bergmann T., Nagar N. M., Robinson A., Lena D., Riffel R. A., Couto G. S., 2014, MNRAS, 437, 1708

Schnorr-Müller A., Storchi-Bergmann T., Robinson A., Lena D., Nagar N. M., 2016, MNRAS, 457, 972

Schönell A. J., Storchi-Bergmann T., Riffel R. A., Riffel R., Bianchin M., Dahmer-Hahn L. G., Diniz M. R., Dametto N. Z., 2019, MNRAS, 485, 2054

Scoville N. Z., Hall D. N. B., Ridgway S. T., Kleinmann S. G., 1982, ApJ, 253, 136

Shimizu T. T. et al., 2019, MNRAS, 490, 5860

Silk J., 2017, ApJ, 839, L13

Singha M. et al., 2022, A&A, 659, A123

Speranza G. et al., 2021, A&A, 653, A150

Speranza G., et al. 2022, A&A, 665, 55

Storchi-Bergmann T., McGregor P. J., Riffel R. A., Simões Lopes R., Beck T., Dopita M., 2009, MNRAS, 394, 1148

Storchi-Bergmann T., Riffel R. A., Riffel R., Diniz M. R., Borges Vale T., McGregor P. J., 2012, ApJ, 755, 87

Storchi-Bergmann T., Schnorr-Müller A., 2019, Nature Astron., 3, 48

Thim F., Hoessel J. G., Saha A., Claver J., Dolphin A., Tammann G. A., 2004, AJ, 127, 2322

Thompson T. A., Fabian A. C., Quataert E., Murray N., 2015, MNRAS, 449, 147

Tonry J. L., Dressler A., Blakeslee J. P., Ajhar E. A., Fletcher A. B., Luppino G. A., Metzger M. R., Moore C. B., 2001, ApJ, 546, 681

Trindade Falcão A. et al., 2021, MNRAS, 500, 1491

Trindade Falcão A. et al., 2021a, MNRAS, 500, 1491

Vivian U. et al., 2019, ApJ, 871, 166

Vayner A. et al., 2021, MNRAS, 504, 4445

Veilleux S., Bolatto A., Tombesi F., Meléndez M., Sturm E., González-Alfonso E., Fischer J., Rupke D. S. N., 2017, ApJ, 843, 18

Veilleux S., Maiolino R., Bolatto A. D., Aalto S., 2020, A&AR, 28, 2

Ward S. R., Harrison C., Costa T., Mainieri V., 2022, MNRAS, 514, 2936

Weinberger R. et al., 2017, MNRAS, 465, 3291

Winge C., Riffel R. A., Storchi-Bergmann T., 2009, ApJS, 185, 186

Wylezalek D. et al., 2017, MNRAS, 467, 2612

Wylezalek D., Flores A. M., Zakamska N. L., Greene J. E., Riffel R. A., 2020, MNRAS, 492, 4680

Xu Y., Luo Y., Kang X., Li Z., Li Z., Wang P., Libeskind N., 2022, ApJ, 928, 100

Yuan W. et al., 2020, ApJ, 902, 26

Yuan W. et al., 2021, ApJ, 913, 3

Zakamska N. L., Greene J. E., 2014, MNRAS, 442, 784

SUPPORTING INFORMATION

Supplementary data are available at *MNRAS* online.

Riffel_Supplementary.pdf

Please note: Oxford University Press is not responsible for the content or functionality of any supporting materials supplied by the authors. Any queries (other than missing material) should be directed to the corresponding author for the article.

This paper has been typeset from a TEX/LATEX file prepared by the author.